



저작자표시-비영리-변경금지 2.0 대한민국

이용자는 아래의 조건을 따르는 경우에 한하여 자유롭게

- 이 저작물을 복제, 배포, 전송, 전시, 공연 및 방송할 수 있습니다.

다음과 같은 조건을 따라야 합니다:



저작자표시. 귀하는 원저작자를 표시하여야 합니다.



비영리. 귀하는 이 저작물을 영리 목적으로 이용할 수 없습니다.



변경금지. 귀하는 이 저작물을 개작, 변형 또는 가공할 수 없습니다.

- 귀하는, 이 저작물의 재이용이나 배포의 경우, 이 저작물에 적용된 이용허락조건을 명확하게 나타내어야 합니다.
- 저작권자로부터 별도의 허가를 받으면 이러한 조건들은 적용되지 않습니다.

저작권법에 따른 이용자의 권리는 위의 내용에 의하여 영향을 받지 않습니다.

이것은 [이용허락규약\(Legal Code\)](#)을 이해하기 쉽게 요약한 것입니다.

[Disclaimer](#)

이학석사 학위논문

전고체전지용 $(100-x)\text{Li}_3\text{SI}-x\text{Li}_6\text{PS}_5\text{Cl}$ ($x=0, 10, 20,$
및 30) 복합고체전해질의 전기화학적 성능 연구

Electrochemical performance of the mixed solid
electrolyte $(100-x)\text{Li}_3\text{SI}-x\text{Li}_6\text{PS}_5\text{Cl}$ ($x=0, 10, 20,$ and
30) for all solid state lithium batteries

울 산 대 학 교 대 학 원

화 학 과

박민호

전고체전지용 $(100-x)\text{Li}_3\text{SI}-x\text{Li}_6\text{PS}_5\text{Cl}$ ($x=0, 10, 20,$
및 30) 복합고체전해질의 전기화학적 성능 연구

Electrochemical performance of the mixed solid
electrolyte $(100-x)\text{Li}_3\text{SI}-x\text{Li}_6\text{PS}_5\text{Cl}$ ($x=0, 10, 20,$ and
30) for all solid state lithium batteries

지도교수 류광선

이 논문을 이학석사 학위 논문으로 제출함

2020年 12月

울산대학교 대학원

화학과

박민호

박민호 의 이학석사 학위 논문을 인준함

심사위원 정 재 훈



심사위원 오 은 석



심사위원 류 광 선



울 산 대 학 교 대 학 원

2020년 12월

감사의글

2018년 11월에 실험실에 들어와 2년 여러 가지 경험을 한 것 같습니다. 우선 2년동안 이끌어주시고 많은 경험과 지식을 쌓게 도와주시고 여러 가지 부족한 면들을 채워주신 교수님께 감사합니다. 또 실험실 생활을 잘 하나갈 수 있게 도와준 영진이, 많은 시간을 함께했고 여러 가지로 도와준 수연이 덕분에 재미있게 실험실 생활해서 즐거웠습니다. 이제 자취 시작해서 꿈에 그리던 자취라이프를 하고 있을 텐데 즐거운 자취생활 하고 거기선 다이어트 성공하길 바랍니다. 그리고 같이 2년동안 생활한 대학원 동기 데오 여러 가지 어려움이 많았지만 잘 마무리 지을 수 있어서 다행입니다. 실험에 대해서 많이 도와주고 신경 써주신 라제시 박사님 감사합니다. 또 얼마 함께 하진 못했지만 유바 박사님도 실험적으로 부족한 부분 자세하게 설명해주시고 도와주셔서 감사합니다. 그리고 질문 무지 많고 항상 물음표를 가지고 다니는 지운이 그만큼 열심히 해주고 여러 가지로 부족했지만 1년동안 잘 생활해줘서 고맙습니다. 저녁은 단백질 우유 같은 것 먹지 말고 푸짐하게 챙겨 드세요. 항상 불평불만 없이 열심히 따라주고 스스로 알아서 열심히 해주고 게임도 잘 하는 학민이 덕분에 백금이 됐어요. 고마워요. 힘들고 어려운 일 있어도 열심히 해서 까꿍이 맛있는 밥 사주세요. 소심한 것 같지만 할 거 다하고 미리 미리 성실하게 공부하는 수정이 내면에 감수성 축축한 아저씨가 살고 있어서 가끔 나오는 소리들이 당황스러웠지만 재미 있었어요. 앞으로도 성실하게 꾸준히 열심히 해요. 여러 가지로 걱정 많이 하지만 지금 이대로 열심히 하면 잘 될 수 있을 거예요. 또 막내라서 그런지 항상 당돌하고 활기찬 금지 웃음 많고 말도 많아서 재미 있었 습니다. 언니 오빠들 말 잘 안 들으면 벽 치기로 정신차리게 하세요. 막내지만 누구보다 똑부러지는 금지 앞으로도 실험실 생활 즐겁게 했으면 좋겠어요. 마지막으로 현아 누나 일 하면서 대학원 생활 하는 게 쉽지 않을 텐데 열심히 하셔서 대단하다고 생각해요. 또 저희가 혹시나 불편해 할 까봐 항상 배려해주셔서 감사해요. 좋은 결과 얻으셔서 잘 졸업하셨으면 좋겠어요. 실험실에 들어와서 지금까지 2년이란 시간이 정말 빠르게 지나갔지만 생각해보면 정말 많은 일들이 있었고 그만큼 즐겁기도 했고 힘들기도 했습니다. 같이 잘 어울려서 생활해주신 모든 분들께 감사드리고 대학원 생활 할 수 있게 지원해준 부모님께 감사드립니다.

Abstract

Li_3OX ($\text{X}=\text{Cl}$, Br , and I) called lithium rich anti-perovskite materials recently reported as super ionic conductors with 3-dimensional Li migrating channels. Li_3OX with anti-perovskite structure as solid electrolytes exhibits the ionic conductivity up to $\sim 10^{-3}$ S/cm and also showing good electrochemical stability due to low interfacial resistance. Li_3OX with anti-perovskite structure as solid electrolytes exhibits thermodynamic stability and shows compatible with lithium metal anode and has a large band gap to hinder electric conductor. These materials have low melting point and high electrochemical stability. But Li_3OX phase tends to decompose into more stable LiX and Li_2O phases at service temperature of interest for LIBs. As the Li_2O phase is a rather poor ionic conductor, it would be useful in examining the feasibility in substitution of O by other chalcogen elements such as S. It is recognized that Li_2S is better ionic conductor than Li_2O . To prevent the decomposition of the substance, Li_3SX ($\text{X}=\text{Cl}$, Br , and I) anti-perovskite was synthesized by replacing S with O.

The $\text{Li}_6\text{PS}_5\text{Cl}$ argyrodite solid electrolyte is known as solid electrolyte with high ionic conductivity of $10^{-2}\sim 10^{-4}$ S/cm⁻¹ at room temperature. Moreover, the high ionic conductivity could be achieved by optimizing the mechanical milling and the annealing processes. However, there is a disadvantage in that electrochemical stability is so lower than Li_3SI .

Based on above studies, we have synthesize $(100-x)\text{Li}_3\text{SI}-x\text{Li}_6\text{PS}_5\text{Cl}$ ($x=0, 10, 20$ and 30) to increase the lithium ionic conductivity and electrochemical stability of them. $\text{Li}_3\text{SI}-\text{Li}_6\text{PS}_5\text{Cl}$ was mixed by milling process. We analyzed the crystal structures of them by XRD. The morphologies, contents, and distribution of the elements in the materials were analyzed by SEM and EDS. As the electrochemical analysis, electrochemical impedance spectroscopy with various temperatures was conducted to evaluate Li^+ conductivity of the materials. Further, the electrochemical performance such as cyclic voltammetry, DC-cycling, and charge and discharge tests were conducted to make synergic effects.

Contents

Acknowledgement -----	4
Abstract -----	5
List of Figures -----	8

Chapter 1. Introduction

1-1. Lithium ion batteries-----	10
1-1-1. Composition of lithium secondary batteries-----	10
1-1-2. Principle of lithium secondary batteries -----	11
1-1-3. Properties and limitation of organic liquid electrolyte-----	12
1-2. Solid electrolyte-----	15
1-2-1. Oxide solid electrolyte -----	15
1-2-1-1. NASICON-----	16
1-2-1-2. Perovskite-----	16
1-2-1-3. Garnet-----	17
1-2-1-4. LISICON-----	19
1-2-2. Sulfide solid electrolyte-----	20
1-2-2-1. Glass-ceramics-----	20
1-2-2-2. Argyrodite-----	21
1-2-3. Lithium rich anti-perovskite -----	22
1-2-3-1. Crystal structure and lithium diffusion mechanism-----	23
1-2-3-2. Anodic stability of lithium rich anti-perovskites-----	27
References -----	30

Chapter 2. General experimental

2-1. Physical characterization -----	39
2.1-1. X-ray diffraction (XRD) -----	39

2-1-2. Field emission scanning electron microscopy & Energy Dispersive Spectrometer (FE-SEM & EDS) -----	41
2-1-3. Laser Raman spectroscopy-----	42
2-2. Electrochemical analysis-----	43
2-2-1. Electrochemical impedance spectroscopy (EIS)-----	43
2-2-2 Cyclic voltammetry (CV) -----	44
2-2-3. Direct current cycling (DC-cycling)-----	44
2-2-4. Galvanostatic charge-discharge measurements (CD)-----	45
References -----	46
Chapter 3 Electrochemical performance of the mixed solid electrolyte (100-x)Li₃Si- xLi₆PS₅Cl (x=0, 10, 20, and 30) for all solid state lithium batteries	
3-1. Introduction -----	47
3-2. Experimental -----	49
3-3. Results and discussion -----	50
3-3-1. Characterization-----	51
3-3-2 Electrochemical analysis-----	54
3-4. Conclusions-----	63
References -----	68
Chapter 4 Summary -----	69

List of Figures

Figure. 1.1 Illustration of operating principle of lithium secondary batteries.

Figure. 1.2 Schematic open-circuit energy diagram of a lithium cell.

Figure. 1.3 Structural schematic of perovskite (LLTO).

Figure. 1.4 Structural schematic of (a) garnet and (b) garnet-related $\text{Li}_5\text{La}_3\text{M}_2\text{O}_{12}$.

Figure. 1.5 Structural schematic of LISICON.

Figure. 1.6 Crystal structures of $\text{Li}_7\text{P}_3\text{S}_{11}$ metastable crystal projected onto the a-c and b-c planes.

Figure. 1.7 Section of the crystal structure $\text{Li}_6\text{PS}_5\text{I}$.

Figure. 1.8 Schematic illustration of structure of lithium rich anti-perovskites.

Figure. 1.9 Schematic illustration of lithium diffusion mechanism in the structure of lithium rich anti-perovskites.

Figure. 1.10 Schematic illustration of lithium diffusion mechanism of by Shockley migration and Frenkel migration.

Figure. 1.11 Schematic illustration of lithium diffusion mechanism of solid electrolyte.

Figure. 1.12 Calculated electrochemical stability window of the solid electrolytes.

Figure. 1.13 Example DC-cycling data of Li_3OCl .

Figure. 1.14 SEM images of $\text{Li}/\text{Li}_2\text{O}/\text{HCl}/\text{Li}$ cell after 160 charge/discharge cycles.

Figure. 2.1 Bragg reflection on a set of atomic planes.

Figure. 2.2 Table of seven crystal system and 14 Bravais lattice.

Figure. 2.3 The Li^+ diffusion mechanism of lithium ion batteries (a), Nyquist plot of an electrode (b), and (c) equivalent circuit from the Nyquist plot.

Figure. 3.1 XRD for $(100-x)\text{Li}_3\text{SI} - x\text{Li}_6\text{PS}_5\text{Cl}$ ($x = 0, 10, 20, \text{ and } 30$).

Figure. 3.2 XRD comparison of $\text{Li}_6\text{PS}_5\text{Cl}$ and $\text{Li}_6\text{PS}_5\text{Cl}$ -ballmill process after annealing.

Figure. 3.3 SEM image for (a) Li_3SI powder, (b) $10\text{Li}_3\text{SI} - 90\text{Li}_6\text{PS}_5\text{Cl}$ powder, (c) $20\text{Li}_3\text{SI} - 80\text{Li}_6\text{PS}_5\text{Cl}$ and (d) $30\text{Li}_3\text{SI} - 70\text{Li}_6\text{PS}_5\text{Cl}$ powder.

Figure. 3.4 Impedance profiles of (a) Nyquist plot for $\text{In} \mid (100-x)\text{Li}_3\text{SI} - x\text{Li}_6\text{PS}_5\text{Cl}$ ($x = 0, 10, 20, \text{ and } 30$) $\mid \text{In}$ symmetric cell (b) Arrhenius plots of the $(100-x)\text{Li}_3\text{SI} - x\text{Li}_6\text{PS}_5\text{Cl}$ materials in temperature range 298.15K to 373.15K .

Figure. 3.5 Cyclic-voltammetry curve of $(100-x)\text{Li}_3\text{SI} - x\text{Li}_6\text{PS}_5\text{Cl}$ materials.

Figure. 3.6 DC cycling of $(100-x)\text{Li}_3\text{SI} - x\text{Li}_6\text{PS}_5\text{Cl}$ materials.

Figure. 3.7 Impedance profiles of (a) Nyquist plot of ASSLB cells before cycling tests and (b) Nyquist plot of ASSLB cells after cycling test.

Figure. 3.8 Initial cycle curve of Li-In alloy $\mid (100-x)\text{Li}_3\text{SI} - x\text{Li}_6\text{PS}_5\text{Cl} \mid \text{Li}(\text{Ni}_{0.8}\text{Co}_{0.1}\text{Mn}_{0.1})\text{O}_2$ in ASSLB.

Figure. 3. 9(a) Cycle performance, (b) capacity retention, and (c) Coulombic efficiency of Li-In alloy $\mid (100-x)\text{Li}_3\text{SI} - x\text{Li}_6\text{PS}_5\text{Cl} \mid \text{Li}(\text{Ni}_{0.8}\text{Co}_{0.1}\text{Mn}_{0.1})\text{O}_2$ in ASSLB.

Chapter 1. Introduction

1-1. Lithium ion batteries

Rechargeable batteries are used in various electronic devices such as laptops, mobile phones, and home appliances. Among commercially available batteries, lithium-ion batteries show the highest energy (250Wh Kg⁻¹), powder density, and long life. Recently, lithium-ion batteries are the subject of intense research aimed at further improving performance and safety at a lower cost to suit higher power densities and more demanding applications. Besides, various studies are being conducted to apply lithium-ion batteries to large-scale energy devices such as electric vehicles (EV), hybrid electric vehicles (HEV), and energy storage systems (ESS). However, the current lithium secondary battery has several disadvantages. First of all, there is the stability issue of the lithium secondary battery. Lithium secondary batteries have safety issues such as the explosion of Samsung and Apple mobile phones in 2016. Also, to apply to electric vehicles, fast charging is required, so a lot of research and effort is required to solve these problems.

1-1-1. Composition of lithium secondary batteries

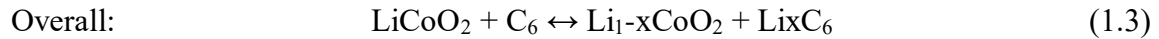
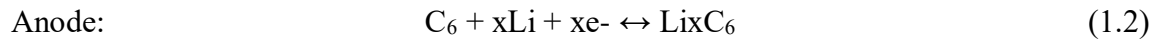
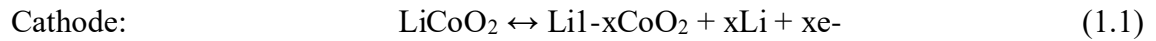
The cathode is made of a mixture of active material, a conductive agent, and a binder coated on a thin Al substrate, and the capacity and voltage of the battery are determined depending on which cathode electrode active material is used. Typical cathode active materials include olivine: LFP (Lithium Iron Phosphate, LiFePO_4) 2-D layered: LCO (Lithium Cobalt Oxide, LiCoO_2), NCA (Lithium Nickel Cobalt Aluminum Oxide, LiNiCoAlO_2), NMC (Lithium Nickel Manganese Cobalt Oxide), $\text{Li}[\text{NiCoMn}]_2\text{O}_2$, 3-D spinel: LMO (Lithium Manganese Oxide, LiMn_2O_4). Like the cathode electrode, the anode electrode is also composed of a Cu base material coated with an active material, and the anode electrode active material reversibly absorbs/discharges lithium ions from the cathode electrode and flows current through an external circuit. Representative anode active materials include Amorphous Carbon, Graphite, Lithium Titanate (LTO, $\text{Li}_4\text{Ti}_5\text{O}_{12}$), and Metallic Anode Materials (Silicon, Tin).

The separator is inserted between both electrodes to prevent short circuits in the battery. It prevents electrons from flowing directly through the electrolyte and allows only desired ions to move through fine pores inside. Currently, commercially available separators include polyolefins such as polyethylene (PE) and polypropylene (PP).

Lastly, the electrolyte serves as a medium for transferring ions, stabilizing the surfaces of the cathode and anode electrodes, and improving the battery life and cell characteristics. It is generally composed of a solvent, salt, and additive. When the solvent is a liquid, it is a liquid electrolyte, a solid electrolyte such as an inorganic compound or a polymer is called a solid electrolyte, and when the solvent is a polymer, it is called a polymer electrolyte. Currently, a liquid electrolyte is most commonly used. In a liquid electrolyte, salt acts as a passage through which lithium ions can move, and LiPF_6 , which has excellent ion mobility, solubility, and chemical stability, is most often used. The solvent plays a role in helping lithium to move smoothly by dissolving salts well. To dissolve the salt well, the solvent must have a high dielectric constant and have low viscosity for the smooth movement of lithium. Besides, the solvent should have low chemical reactivity because it may cause safety problems when reacting with the anode and the cathode while the battery is operating. Usually, Ethylene Carbonate (EC) is most often used as a solvent. The additive is first decomposed so as not to decompose the solvent, thereby forming a protective film on the surface of the cathode or anode electrode, helping lithium to move smoothly between the cathode electrode and the anode electrode and preventing deterioration of battery performance. The electrolyte must be chemically and electrically stable so as not to cause side reactions to degrade the battery's performance during operation and must have a low freezing point and a high boiling point so that the battery can operate at any time.

1-1-2. Principle of lithium secondary batteries.

The operating principle of a lithium secondary battery is presented in Figure 1.1. For example, at the charging step, the cathode and anode materials are oxidized and reduced respectively first. The chemical reactions during charging and discharging can be represented as follows equation.



Throughout this chemical reaction, the electrons move through the external circuit connected to the current collectors to anode materials and make them reduce. After the chemical reaction of two electrode materials, lithium ions are released from the cathode to maintain the electronic charge neutrality of the materials. The ions released are diffused and intercalated to the surface and the structure of an anode is reduced by accepting electrons. During this step, chemical energy made by the chemical reaction can be converted and stored to electronic energy by following the Nernst equation (eq. 1.4).

$$\Delta G = -nFE \quad (1.4)$$

Where G is Gibbs energy, n is the number of electrons, F is Faraday's constant number, and E is electric potential. This equation means that electric potential energies are proportional to chemical energies, which means that large chemical potential difference between cathode and anode induce large electric potential and energy. The electric potential proportioning to chemical energies are called to open-circuit voltage (OCV) and is determined within the bandgap of the electrolyte, which is determined the energy difference between the highest occupied molecular orbital (HOMO) and the lowest unoccupied molecular orbital (LUMO) of the electrolyte in Figure 1.2 [1-3].

1-1-3. Properties and limitation of organic liquid electrolyte

Commercial organic liquid electrolytes consist of a mixture of two or more carbonate-based materials and a lithium salt such as ethyl carbonate (EC)/di-methyl carbonate (DMC)=1:1 in 1M LiFP₆. The electrolytes have been applied to many lithium based batteries due to its good dielectric constant and electrochemical stability compare with aqueous electrolyte. But, in order to be applied to a large scale energy devices, the electrolytes must be satisfy several requirements such as : [4]

- 1) Retention of the SEI during charge and discharge.
- 2) A Li⁺ ion conductivity $\sigma_{Li} > 10^{-4} S/cm$.
- 3) An electronic conductivity $\sigma_e < 10^{-10} S/cm$.
- 4) A transference number $\sigma_{Li}/\sigma_{total} \approx 1$, where σ_{total} includes conductivities by other ions in the electrolyte.
- 5) Chemical stability over wide temperature ranges.

Among these requirements, there are conditions that the organic electrolyte not meet such as low transference number, chemical stability, and electrochemical stability. Usually, lithium salt electrolytes have showed a low transference number of lithium ions (0.3~0.5/l) which occur a poor high-rate performances and limits the powder output of the cell [1] because of their dielectric mechanism such as solvation and dissociation. However, the most important thing to solve is safety related with thermal stability and leakage of the liquid types. As the organic electrolytes are decomposed and occur high thermal energy at high temperature, the lithium batteries expand and induce shrinkage of the membrane. And finally, the short between cathode and anode occurs and leads to explosion. To solve these problems, various type of electrolytes have been developed such as gel-type and solid state electrolyte due to their no leak properties and good thermal and electrochemical stability.

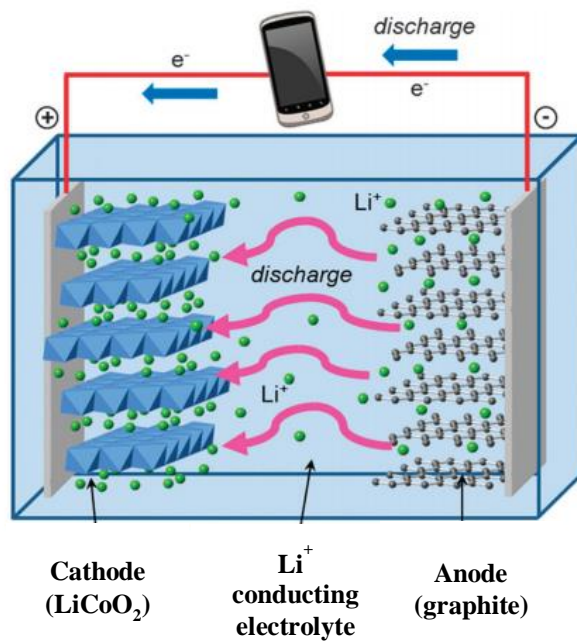


Figure 1.1. Illustration of operating principle of lithium secondary batteries.

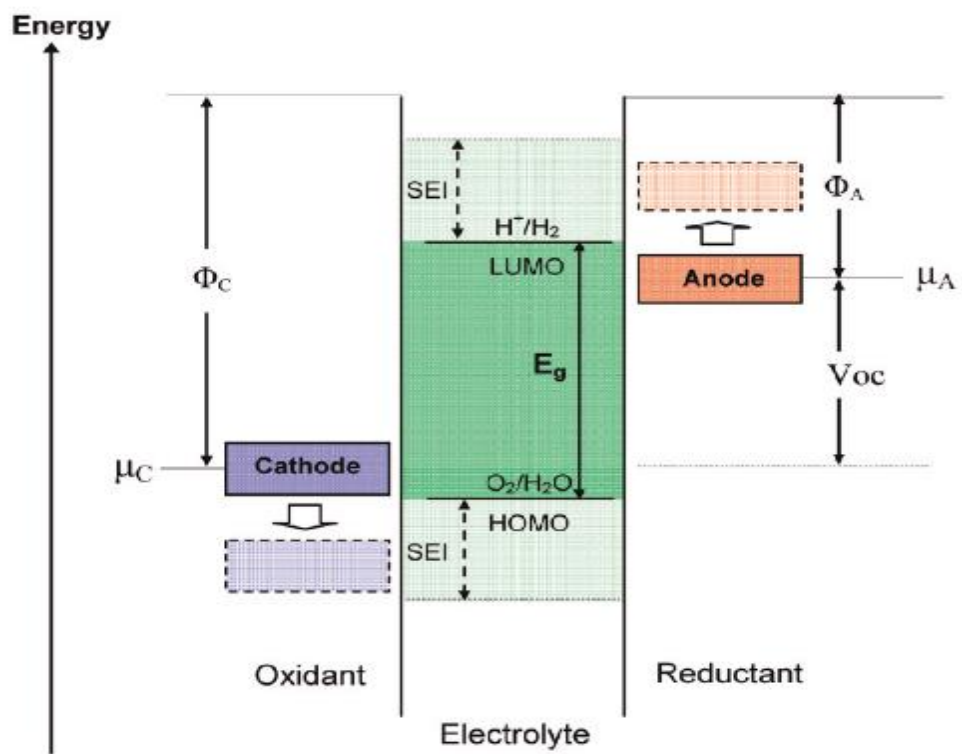


Figure 1.2. Schematic open-circuit energy diagram of a lithium cell.

1-2. Solid electrolytes

Lithium-ion batteries have been widely used as rechargeable power sources for portable electronics and large-scale devices such as cell phones, laptop computers, and hybrid electronic vehicles [5]. Usually, the traditional organic liquid electrolytes used in lithium-ion batteries come with serious problems due to risks of leakage and flammability [6]. Therefore, the replacement of liquid electrolytes with a solid electrolyte could enhance the electrochemical performance, safety, reliability of these batteries as well as give a higher energy density [7]. Moreover, solid electrolytes have received much interest due to their potential for good ionic conductivity and a high lithium transference number (~ 1) compared to aprotic electrolytes (0.2~0.5) [8, 9]. Among these advantages, the solid electrolytes for large scale electric devices have been intensively studied due to its attractive advantages for the safety of lithium secondary batteries such as its electrochemical and thermal stability [1, 2]. The solid electrolytes are widely divided into ceramics and polymers. In the case of polymer electrolytes, they have good flexibility and also can be flexible batteries and devices. However, the poor mechanical properties and low ionic conductivity offset these electrolytes from practical applications. Therefore, recently many researchers have been studying ceramic solid electrolytes.

1-2-1. Oxide solid electrolyte

Most oxide-based solid electrolytes produced have focused on using NASICON, perovskite, garnet, and LISICON structures. The NASICON structures such as $\text{Li}_{1.3}\text{Al}_{0.3}\text{Ti}_{1.7}(\text{PO}_4)_3$ have a high electrochemical oxidative voltage window ($\sim 6\text{V}$ versus Li^+/Li) [15] as well as stability from air and moisture. However, the NASICON electrolytes containing Ti are unstable with Li metal at low potentials. The perovskite such as $\text{Li}_3\text{La}_{(2/3-x)}\text{d}_{(1/3)-2x}\text{TiO}_3$ (LLTO, $0 < x < 0.16$), is representative material due to its high ionic conductivity at room temperature (10^{-3} S/cm). In the case of the garnet structure, the grain boundaries can go through dendrite and have large interfacial resistance due to their being no wet surface next to the Li metal [16]. The LISICON structures such as $\text{Li}_{3x}\text{La}_{2/3-x}\text{TiO}_3$ and $\text{Li}_{3/8}\text{Sr}_{7/16}\text{Zr}_{1/4}\text{Ta}_{3/4}\text{O}_3$, have low contact with Li metal due to the reduction of Ti and Ta ions

[16].

1-2-1-1. NASICON

NASICON-like structures are generally known as a rhombohedral unit cell and $R\bar{3}c$ with a few monoclinic and orthorhombic phases [17]. Representatively, $L_{1+6x}M_{4+2-x}M'_{3+x}(PO_4)_3$ phosphates (L = Li or Na and M = Ti, Ge, Sn, Hf, or Zr and M' = Cr, Al, Ga, Sc, Y, In, or La) are composed with MO_6 octahedra connected by corner-sharing with PO_4 tetrahedral to form 3D interconnected channels and two types of interstitial positions where mobile cations are distributed in the Figure. 1.3 [18]. The M_1 sites which are 6-fold coordination located between two MO_6 octahedral while M_2 sites that are 8-fold coordinated and located between two columns of MO_6 octahedra [19]. The lithium ions diffuse from one site to another through bottlenecks.

NASICON-like materials $LiA_2IV(PO_4)_3$ showed ionic conductivity 10^{-5} S/cm at room temperature in 2009 [20]. To solve the size mismatch between Li^+ and TiO_6 octahedral, a few materials have been developed and exhibited improved ionic conductivity such as the $Li_{1.3}Al_{0.3}Ti_{1.7}(PO_4)_3$ (10^{-3} S/cm) [21]. Also, the materials have a high electrochemical oxidative voltage window ($\sim 6V$ versus Li^+/Li) [15] as well as stability from air and moisture. However, the NASICON electrolytes containing Ti are unstable with Li metal at low potentials.

1-2-1-2. Perovskite

Perovskite materials having chemical formula ABO_3 is well known as the representative cubic phase with space group $Pm\bar{3}m$. Among the structural materials, lithium-lanthanum-titanates, $Li_3La_{(2/3)-x}d_{(1/3)-2x}TiO_3$ (LLTO, $0 < x < 0.16$), is representative material due to its high ionic conductivity at room temperature (10^{-3} S/cm) [10]. The crystal structure of the LLTO is in Figure 1.4 [20]. The A-site cations, which were Li^+ and La^{3+} in the cubic α -phase, were randomly distributed, while the A sites of the ordered β -LLTO had a doubled perovskite structure, with an alternating arrangement of La^+ rich and Li vacancy rich layers along the c axis [21]. Not only high ionic conductivity, but the materials also have many advantages such

as stability in air and moisture, wide stability temperature window (to 1600K), good electrochemical stability (>8V). However, the materials have not been applied to commercial solid battery system because of its unsuitable for use with lithium and graphite negative electrodes [3, 10], high-temperature sintering for synthesis, lower ionic conductivity than that of the single crystal due to tot blocking grain boundaries [15, 22].

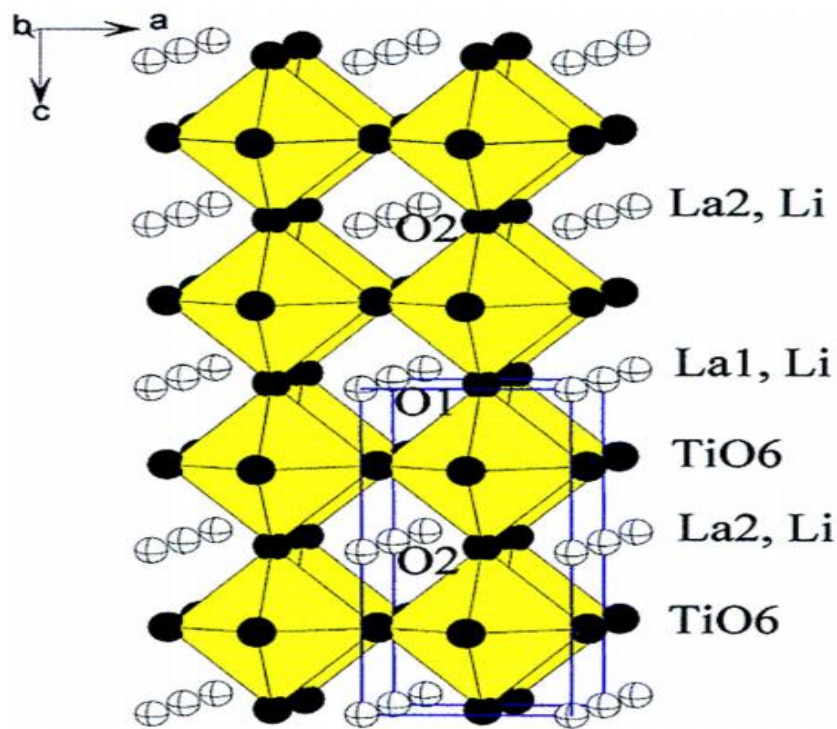


Figure 1.3 Structural schematic of perovskite (LLTO).

1-2-1-3. Garnet

The garnets exhibit a general chemical formula of $A_3B_2(XO_4)_3$ (A = Ca, Mg, Y, La or rare-earth; B = Al, Fe, Ga, Ge, Mn, Ni or X = Si, Ge, Al) where A, B, and C are eight, six and four oxygen coordinated cation sites, which crystalize in a face-centered cubic structure with the

space group $Ia\bar{3}d$ (Figure 1.5) [23]. Because the garnet electrolytes high Li^+ concentration of 5~7 Li atoms per formula unit and can accommodate excess Li^+ at octahedral sites than that of the number of lithium at the tetrahedral sites [23], the ionic conductivity of the electrolytes can be controlled by increasing Li concentration. For example, $\text{Li}_5\text{La}_3\text{M}_2\text{O}_{12}$ has a low ionic conductivity of 10^{-6} S/cm at room temperature. However, the low conductivity can be improved when La and M sites are substituted with cations of higher or lower oxidation state than La^{3+} and M^{5+} with controlling the content of substitution elements such as $\text{Li}_{6.6}\text{La}_3\text{Zr}_{1.6}\text{Sb}_{0.4}\text{O}_{12}$ (7.7×10^{-4} S/cm) and $\text{Li}_{6.2}\text{La}_3\text{Zr}_{1.2}\text{Sb}_{0.8}\text{O}_{12}$ (4.5×10^{-4} S/cm) [24,25]. Also, the ionic conductivity of the garnet electrolytes can be improved by controlling shape control. For example, the particle shape of $\text{Li}_7\text{La}_3\text{Zr}_2\text{O}_{12}$ changes by contents of the substitution element (Ga), and can be more dense pellets with the same pressure [26]. As a result, the interface resistance by grain boundary was reduced.

Although garnet electrolytes have high lithium concentration and ionic conductivity, the materials couldn't be commercialized because of their unstable reactivity with cathode materials at the positive voltage window [27].

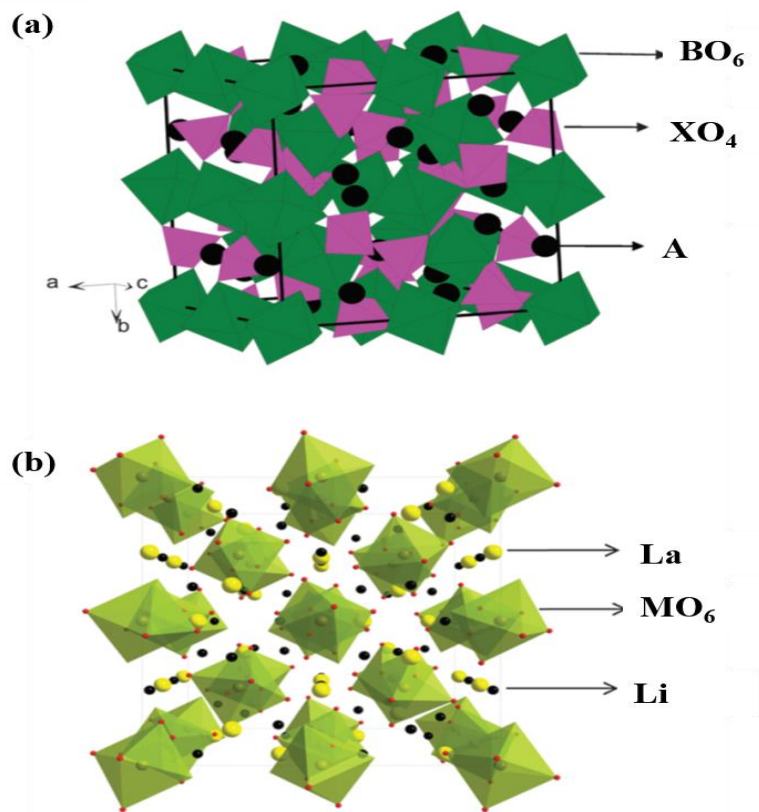


Figure 1.4 Structural schematic of (a) garnet and (b) garnet-related $\text{Li}_5\text{La}_3\text{M}_2\text{O}_{12}$.

1-2-1-4. LISICON

The crystal structure of LISICON-like compounds is related to the $\gamma\text{-Li}_3\text{PO}_4$ structure with an orthorhombic unit cell and pnma space group, where all cations are tetrahedrally coordinated [10,28]. The oxide LISICON-like materials such as $\text{Li}_{14}\text{ZnGe}_4\text{O}_{16}$ showed low ionic conductivity ($\sim 10^{-7}$ S/cm) at room temperature by trapping of the mobile Li^+ ions by the immobile sublattice at lower temperatures via the formation of defect complexes [20]. Recently, the thio-LISICON changed O^{2-} to S^{2-} have been studied for high lithium-ion conductivity by 3 orders of magnitude at room temperature [10]. Many thio materials such as $\text{Li}_{10}\text{MP}_2\text{S}_{12}$ ($\text{M}=\text{Si}, \text{Ge},$ and Sn), $\text{Li}_{11}\text{Si}_2\text{PS}_{12}$ showed high ionic conductivity [29-31]. Especially, $\text{Li}_{10}\text{GeP}_2\text{S}_{12}$ showed highest lithium-ion conductivity ($\sim 10^{-2}$ S/cm) at 27°C [29] among current ceramic electrolytes (Figure. 9) [10]. As the radius of S^{2-} is higher than O^{2-} , this substitution can significantly enlarge the size of Li^+ transport bottlenecks. Also, S^{2-} has

better polarization capability than O^{2-} . Consequently, the interaction between a skeleton and Li^+ ions is weaker and makes the mobility of Li^+ [32]. The thio-LISICON materials also have a favorable advantage, which is the reduction of grain boundary resistance by simple cold-press of electrolytes powders because of its good ductility compare with hard oxide materials [20].

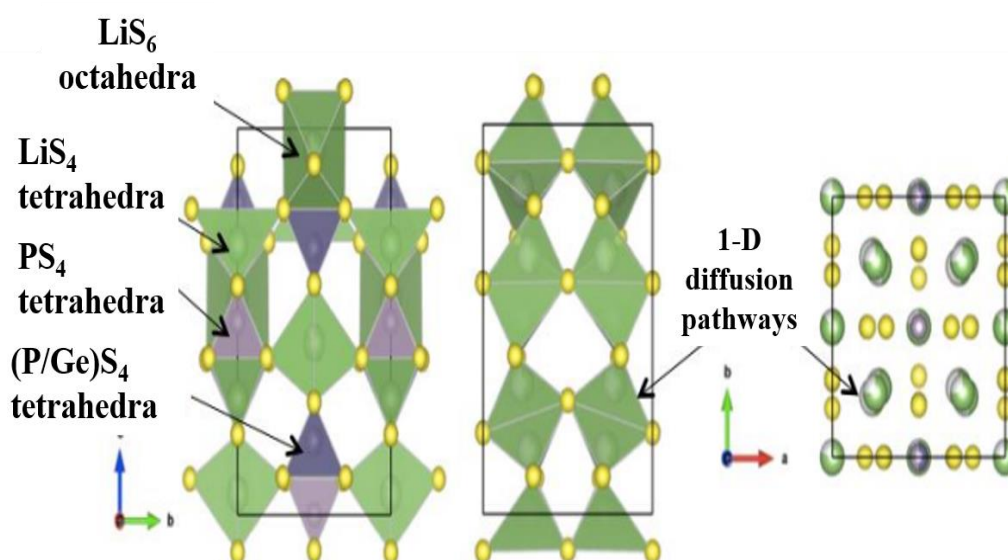


Figure 1.5 Structural schematic of LISICON

1-2-2. Sulfide solid electrolyte

Sulfide-based solid electrolytes have a smaller grain boundary and higher ionic conductivity compared with oxide-based electrolytes due to the high polarizability of sulfur ions and their low binding force with lithium ions [33, 34]. In particular, the sulfide solid electrolyte has received a lot of attention because it has a high conductivity ($\sim 10^{-4} S/cm$) comparable to that of a liquid electrolyte among solid electrolytes. Sulfide-based solid electrolytes derived from oxide-based solid electrolytes are formed by replacing oxygen ions with sulfur ions.[68] Even the ionic migration of S^{2-} is larger than that of O^{2-} due to the large ionic radius of S^{2-} compared to O_2 [35]. Depending on the crystal structure and composition, sulfide solid electrolytes are classified into $Li_2S-P_2S_5$ glass and glass ceramics, and anion-doped $Li_2S-P_2S_5$, argyrodite, etc. [69] Actually, almost thio materials react and are

decomposed with cathode materials and anode materials including Li metal [46, 47]. In addition, the materials are difficult to synthesis in the general atmosphere because they are very sensitive to air and moisture.

1-2-2-1. Glass-ceramics

The representative solid electrolyte of glass-ceramics is a solid electrolyte called LPS based on $\text{Li}_2\text{S-P}_2\text{S}_5$. $\text{Li}_2\text{S-P}_2\text{S}_5$ based glass-ceramics are of special interest because of its high ionic conductivity of up to 1.7×10^{-2} S/cm at room temperature and its wide electrochemical window [36 - 40]. In addition to the advantages described above $\text{Li}_7\text{P}_3\text{S}_{11}$ (LPS) glass-ceramic can be synthesized easily by methods such as ball milling and by solution techniques where another component can be mixed with the LPS [41, 42]. One synthesis method used mechanical wet milling with solvent to acquire the solid electrolyte $\text{Li}_7\text{P}_3\text{S}_{11}$ which showed particularly high ionic conductivity. Moreover, after heat treatment, obtained powders can be applied easily in the fabrication of electrolytes for bulk type ASSLBs [43]. However, LPS has large interfacial resistance with lithium metal, which restricts its application in an all-solid-state battery. This characteristic results in low coulombic efficiency and degradation of capacity in an all-solid-state battery due to the reaction between the LPS and Li metal [41]. Even the $\text{Li}_2\text{S-P}_2\text{S}_5$ system can generate H_2S gas in the case of a reaction with any moisture which is why the system is thought to have low chemical stability.

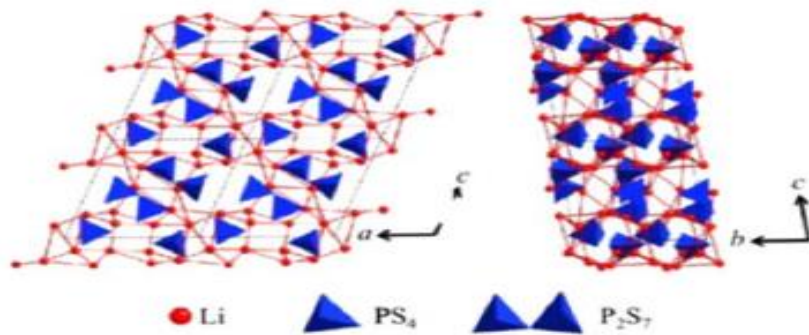


Figure 1.6 Crystal structures of $\text{Li}_7\text{P}_3\text{S}_{11}$ metastable crystal projected onto the a-c and b-c planes

1-2-2-2. Argyrodite

An Argyrodite-type Li-ion solid electrolyte is typically $\text{Li}_6\text{PS}_5\text{X}$ ($\text{X} = \text{Cl}, \text{Br}, \text{I}$). It has a structure similar to Cu^+ and Ag^+ argyrodites. Six sulfur and halogen atoms form 136 tetrahedral pores, of which four are formed only by the sulfur atom (S1) and occupied by the P atom. The remaining 132 holes are formed by a sulfur atom (S2) and a halogen atom (X), partially occupied by a Li atom.[71]. $\text{Li}_6\text{PS}_5\text{X}$ ($\text{X} = \text{Cl}, \text{Br}, \text{I}$) argyrodite solid electrolyte exhibits very high ionic conductivity at room temperature, but it has a disadvantage that its capacity decreases significantly in more than 20 cycles in the battery charge/discharge test. also similar to other sulfide-type solid electrolytes, argyrodite-type solid electrolytes could not be exposed to air, which restricts its application to a large extent. Effective and convenient battery construction technologies are required to conquer the stability problems.[70]

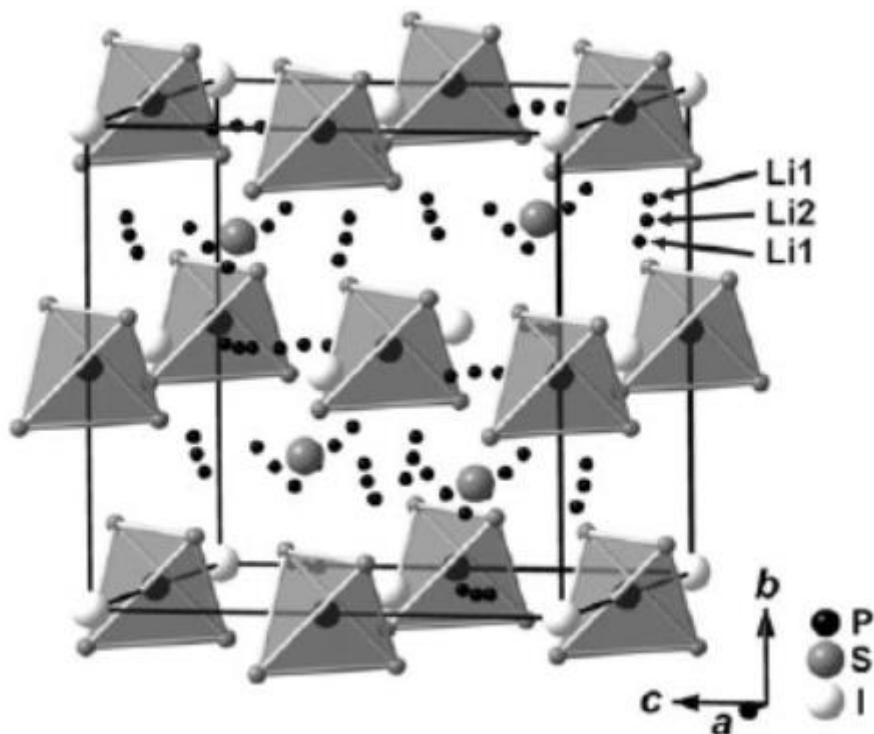


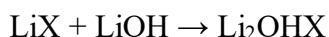
Figure 1.7 Section of the crystal structure $\text{Li}_6\text{PS}_5\text{I}$

1-2-3. Lithium rich anti-perovskite

An antiperovskite material with the formula M_3AX (M, transitional metal; A, metal or semiconducting element and X, interstitial light element) has been developed and applied to a few fields. Various beneficial properties including magneto volume effects [48], magnetostriction [49], magnetocaloric effects [50], magnetoresistance [51], low-temperature coefficients [52, 53], functional mechanical properties, and superconductivity have been obtained in antiperovskites. Recently, A_3BO type ($\text{A} = \text{M}^{+1}$ alkali metal, $\text{B} = \text{X}^{-1}$ anion, and oxygen) such as Na_3OX and Li_3OX materials have been received attention as the superionic solid electrolytes [54]. This class of solid electrolytes exhibit Li conductivities on the order of 1 mS/cm, with a maximum conductivity of 1.94 mS/cm achieved for a solid solution mixture of Li_3OCl and Li_3OBr [54, 55] because of the simple cubic-like structure and beneficial properties, the materials have been applied to various studies. Among the characteristics of the antiperovskites, the best of the advantage is stable with lithium anode. In this section, we introduce the antiperovskite materials for lithium superionic conductors for lithium secondary

batteries and explain our experimental purpose.

Recently, superionic conductivity in Li-rich antiperovskites such as Li_3OX and Li_2OHX ($X = \text{Cl}, \text{Br}$) have received attention as a potential new solid electrolyte in Li secondary batteries. [56 - 63]. Li_2OHX ($X = \text{Cl}, \text{Br}$) has many advantages that are stable in contact with Li metal and a wide energy window up to 9V (vs. Li^+/Li) [56]. Comparison with Li_3OX types, the best advantage of Li_2OHX is easy and simple synthesis. The products are usually produced by solid-state synthesis as followed by the equation.

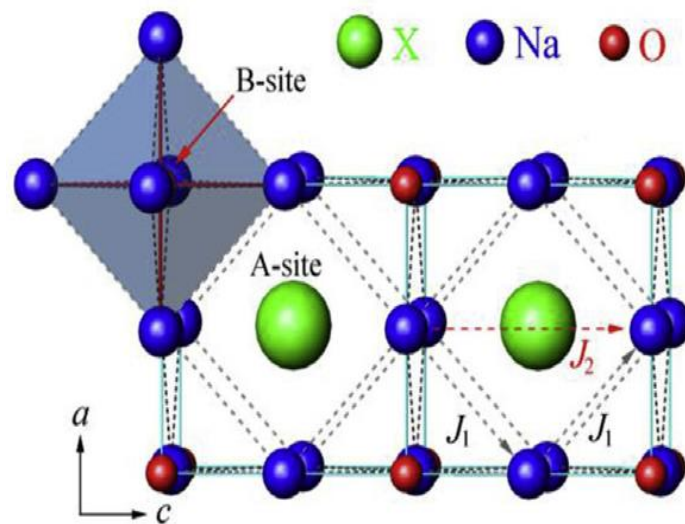


The synthesis for Li_2OHX is required only one grinding or ball-mill and calcination with low temperature (300~350°C) and a short time (30min~4h). Because the Li_2OHX materials are stable at room temperature unlike Li_3OX type, the materials are easy to handling and synthesis. Also, the pseudo-anti-perovskites have a self-stabilizing characteristic similar to Li_3OX . Figure 1.12 and 1.13 shows the results of cross-section SEM images and DC-cycling of $\text{Li}_2\text{OHCl}/\text{SEI}/\text{Li}$. As a results, the electrochemical stability versus Li is stable and the materials form stable SEI during cycling. However, Li_2OHX ($X = \text{Cl}, \text{Br}$) materials display low ionic conductivity at room temperature ($10^{-7}\sim 10^{-6} \text{ Scm}^{-1}$) because Li^+ migration is interrupted by coulombic repulsion and steric hindrance from the H^+ ion in the fixed O-H bonds of the hydroxide ion [56].

1-2-3-1. Crystal structure and lithium diffusion mechanism

The Li_3OX antiperovskite materials were developed by replacing the electronegative anion element in the traditional perovskite system by the electropositive lithium metal, and continue the electronic inversion to $X^-\text{O}^{2-}\text{Li}^{+13}$, where monovalent anion (halogen), O^{2-} , and Li^+ . Figure 1.7 shows the crystal structure of antiperovskite Li_3OX ($X=\text{Cl}, \text{Br}$) with cubic symmetry and space group $\text{pm}3\text{m}$ [64]. OLi_6 octahedra share their corners with each other to form a three-dimensional framework (B-site) and the halogen anions occupy the 12-coordinated dodecahedral center A-site. Unlike usual solid electrolyte having substantial disorder and high vacancy concentration due to incomplete filling of particular crystallographic sites and thermodynamic effect [57, 64], The lithium-rich antiperovskite materials consist of highly ordered Li sublattices. Therefore, Li migration is mediated by defects including Li vacancy (Shockley style) and interstitials (Frenkel style) [57]. Because

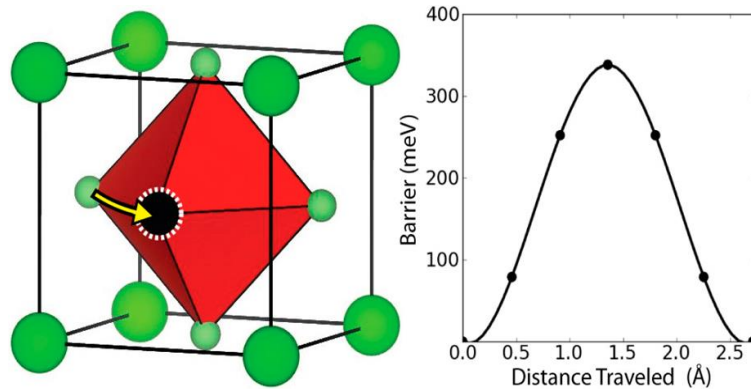
the main migration is separated with two factors, the activation energy for Li^+ migration is also different from the migration mechanism. The results of the calculated energy are that the Li migration into a vacancy is 340 meV and the migration of interstitial is 145 meV in Li_3OCl crystal. As the result, the Li migration in Li_3OX crystal prefers the Frenkel migration than the shockkey style. Figure 1.9 shows lithium migration illustration by Frenkel migration. When a Li atom from an octahedron moves to an interstitial site leaving behind vacancy, the excess Li prefers to form a dumbbell configuration with a Li of an octahedron. The center of the dumbbell resides at the octahedron corner of the displaced Li-ion. The stable orientations of the Li dumbbell are parallel to the cubic axes of the perovskite crystal [57].



- Cubic type (pm3m)
- B site $\rightarrow \text{Li}_6\text{O}$ (Oxygen in O_h)
- A site \rightarrow halogen site (dodecahedral site)

Figure 1.8 Schematic illustration of structure of lithium rich anti-perovskites.

1. Shokkey migration: vacancy \rightarrow vacancy (Li ion pathway)



2. Frenkel migration: interstitial \rightarrow interstitial

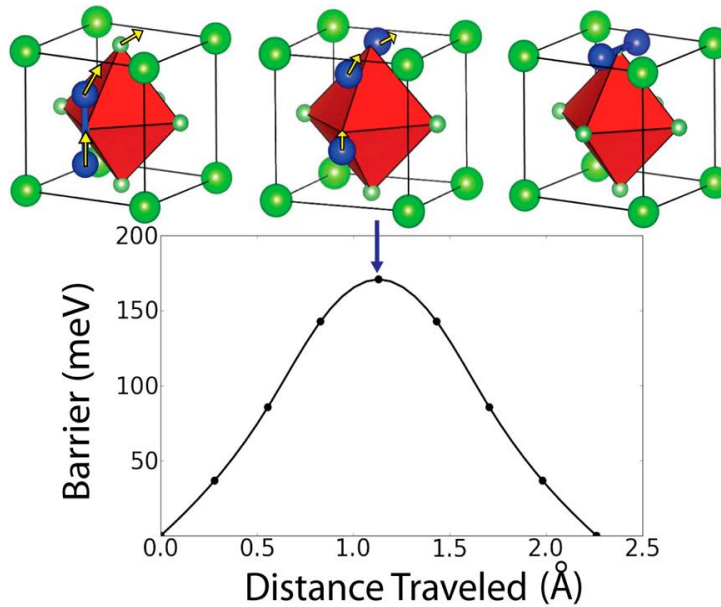


Figure 1.9 Schematic illustration of lithium diffusion mechanism in the structure of lithium rich anti-perovskites.

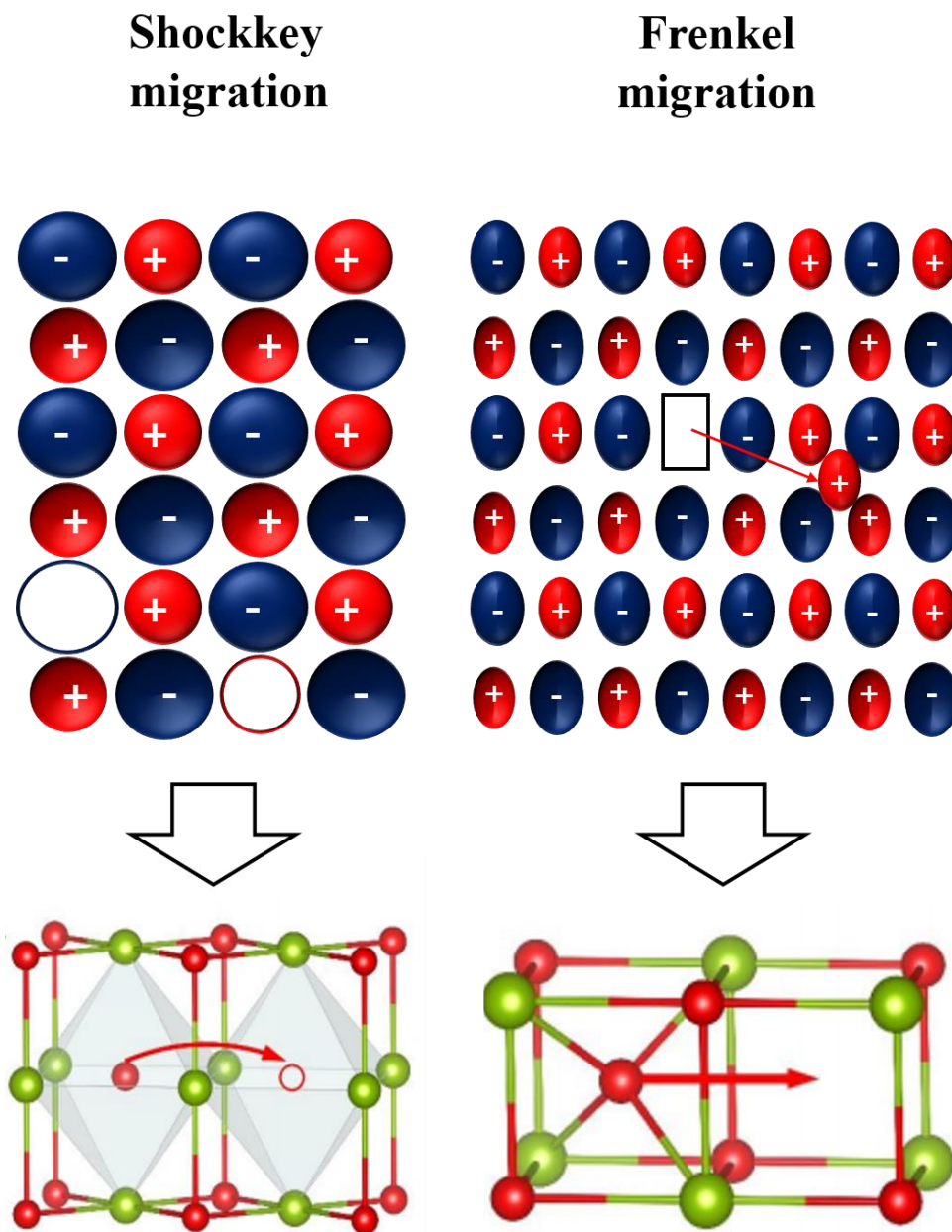


Figure 1.10 Schematic illustration of lithium diffusion mechanism of by Shockley migration and Frenkel migration.

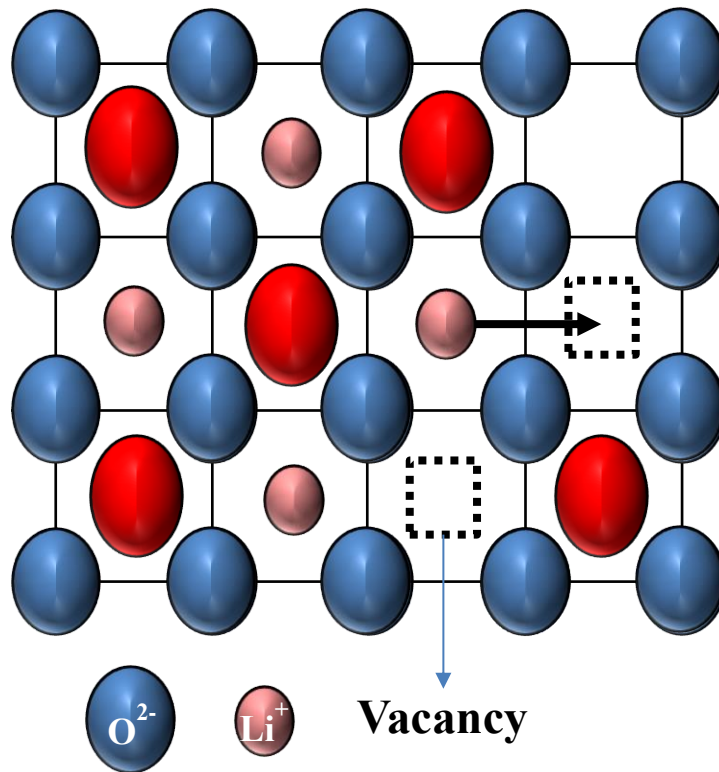


Figure 1.11 Schematic illustration of lithium diffusion mechanism of solid electrolyte.

1-2-3-2. Anodic stability of lithium-rich antiperovskites

One of the effective physical properties of lithium-rich antiperovskites is stable with lithium anode [65]. The stable electrochemical window of Li_3OCl is listed in Figure. 1.11. Compare with sulfide materials, the theoretical voltage window of the antiperovskites is in at stable anodic voltages from 0V to 3V versus Li/Li^+ . The theoretical calculation explains that the antiperovskite materials are almost not reacted with an anode such as graphite, $\text{Li}_4\text{Ti}_5\text{O}_{12}$, and Li metal. Figure 1.12 exhibits example data of DC-cycling of Li_3OCl (direct current-cycling) [66]. DC-cycling is a measurement for the investigation of correct electrochemical stability versus Li metal. The measurement is conducted as contacting between Li and solid electrolyte using the symmetric cell of $\text{Li}/\text{electrolyte}/\text{Li}$ by applying a constant direct-current (DC) with periodically changed polarity [66, 67]. Compare with unstable LGPS, the antiperovskite material such as Li_2OHBr , Li_3OCl showed a stable voltage profile. Except for

initial cycling, the voltage changes which means reactivity with Li almost not occurs during the cycling. This means that the electrolyte has good electrochemical stability. In the case of voltage change during the initial cycle, Li_3OCl react with Li metal and form stable SEI via self-stabilizing feature such as Al_2O_3 formation on Al aluminum to protect the metals from oxidation. Because of this physical characteristic, lithium-rich antiperovskites can be promising candidates for ASSLB.

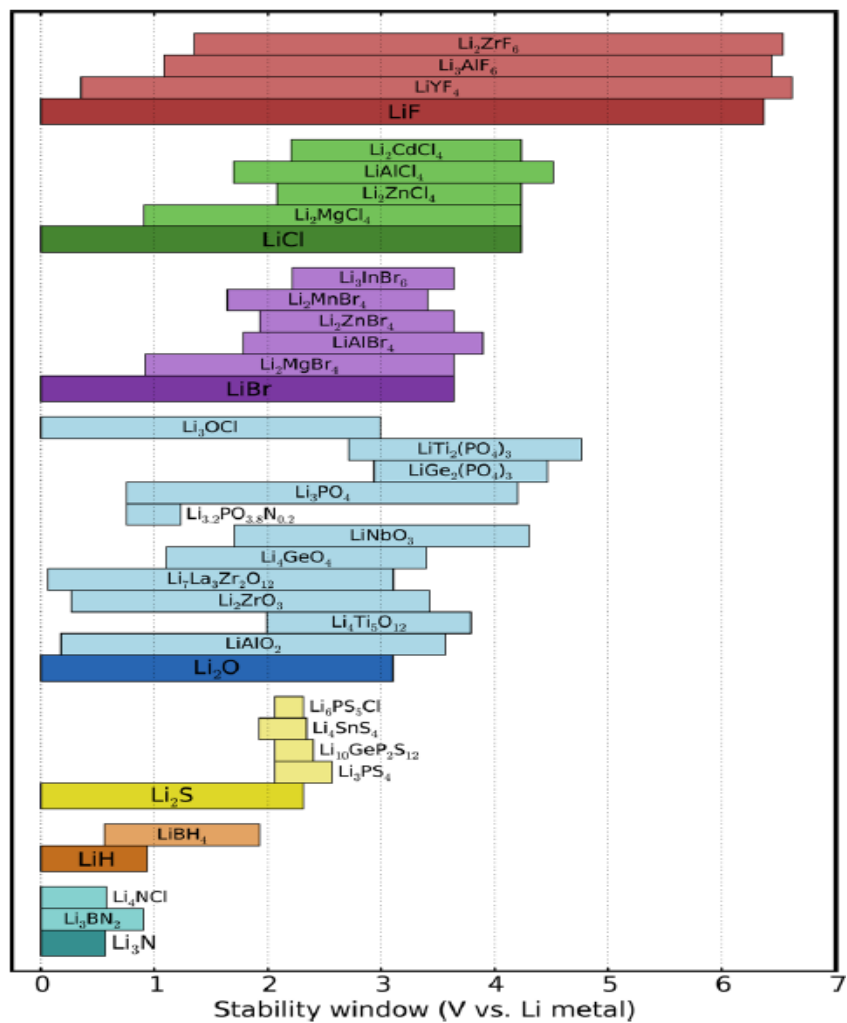


Figure 1.12 Calculated electrochemical stability window of the solid.

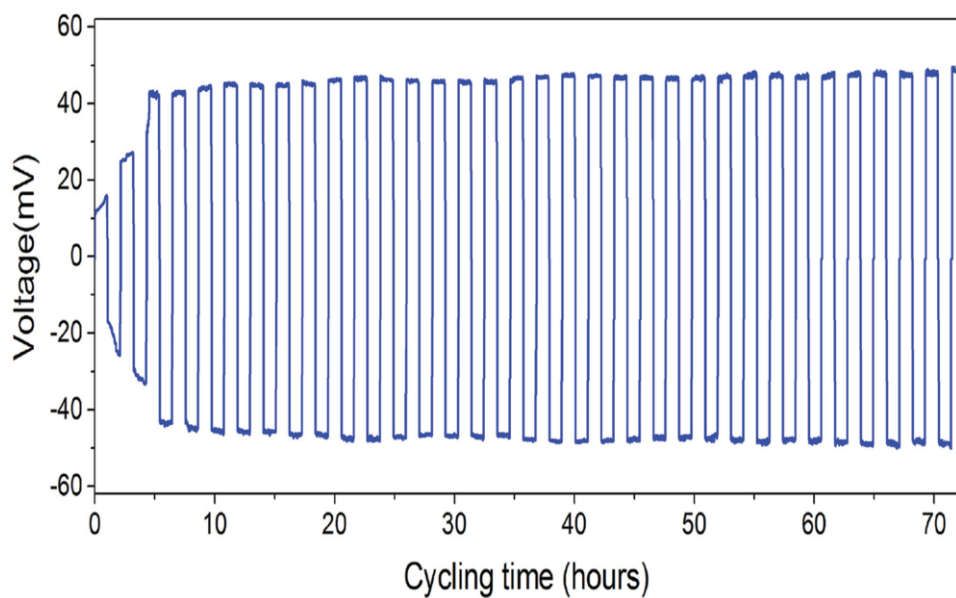


Figure 1.13 Example DC-cycling data of Li_3OCl .

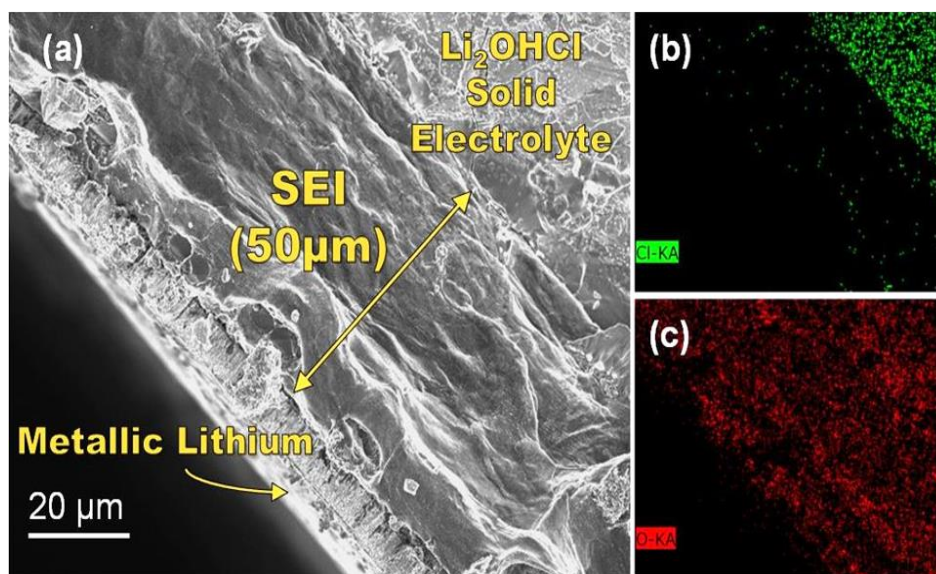


Figure 1.14 SEM images of $\text{Li}/\text{Li}_2\text{OHCl}/\text{Li}$ cell after 160 charge/discharge cycles.

Reference

- [1] Minh, Nguyen Q. "Ceramic fuel cells." *Journal of the American Ceramic Society* 76, no. 3 (1993): 563-588.
- [2] Tarascon, J-M., and Michel Armand. "Issues and challenges facing rechargeable lithium batteries." In *Materials for sustainable energy: a collection of peer-reviewed research and review articles from Nature Publishing Group*, pp. 171-179. 2011.
- [3] Stephan, A. Manuel, and K. S. Nahm. "Review on composite polymer electrolytes for lithium batteries." *Polymer* 47, no. 16 (2006): 5952-5964.
- [4] Xu, Kang. "Nonaqueous liquid electrolytes for lithium-based rechargeable batteries." *Chemical reviews* 104, no. 10 (2004): 4303-4418.
- [5] Seino, Yoshikatsu, Tsuyoshi Ota, Kazunori Takada, Akitoshi Hayashi, and Masahiro Tatsumisago "A sulphide lithium super ion conductor is superior to liquid ion conductors for use in rechargeable batteries" *Energy & Environmental Science* 7, no. 2 (2014): 627-631.
- [6] Zhang, Jicheng, Rui Gao, Limei Sun, Heng Zhang, Zhongbo Hu, and Xiangfeng Liu "Unraveling the multiple effects of Li_2ZrO_3 coating on the structural and electrochemical performances of LiCoO_2 as high-voltage cathode materials" *Electrochimica Acta* 209 (2016): 102-110.
- [7] Wenzel, Sebastian, Dominik A. Weber, Thomas Leichtweiss, Martin R. Busche, Joachim Sann, and Jürgen Janek "Interphase formation and degradation of charge transfer kinetics between a lithium metal anode and highly crystalline $\text{Li}_7\text{P}_3\text{S}_{11}$ solid electrolyte." *Solid State Ionics* 286 (2016): 24-33.
- [8] Xu, Kang "Nonaqueous liquid electrolytes for lithium-based rechargeable batteries" *Chemical Reviews* 104, no. 10 (2004): 4303-4418.
- [9] Kamaya, Noriaki, Kenji Homma, Yuichiro Yamakawa, Masaaki Hirayama, Ryoji Kanno, Masao Yonemura, Takashi Kamiyama, Yuki Kato, Shigenori Hama, Koji Kawamoto and

- Akio Mitsui "A lithium superionic conductor" *Nature Materials* 10, no. 9 (2011): 682.
- [10] Bachman, John Christopher, Sokseiha Muy, Alexis Grimaud, Hao-Hsun Chang, Nir Pour, Simon F. Lux, Odysseas Paschos et al. "Inorganic solid-state electrolytes for lithium batteries: mechanisms and properties governing ion conduction." *Chemical reviews* 116, no. 1 (2016): 140-162.
- [11] Goodenough, John B., and Youngsik Kim. "Challenges for rechargeable Li batteries." *Chemistry of materials* 22, no. 3 (2010): 587-603.
- [12] Dyer, Chris K., Patrick T. Moseley, Zempachi Ogumi, David AJ Rand, and Bruno Scrosati, eds. *Encyclopedia of Electrochemical Power Sources*. Elsevier Science & Technology., 2009.
- [13] Jung, Yun-Chae, Seul-Ki Kim, Moon-Sung Kim, Jeong-Hye Lee, Man-Seok Han, Duck-Hyun Kim, Woo-Cheol Shin, Makoto Ue, and Dong-Won Kim. "Ceramic separators based on Li⁺-conducting inorganic electrolyte for high-performance lithium-ion batteries with enhanced safety." *Journal of Power Sources* 293 (2015): 675-683.
- [14] Garche, Jurgen, Chris K. Dyer, Patrick T. Moseley, Zempachi Ogumi, David AJ Rand, and Bruno Scrosati, eds. *Encyclopedia of electrochemical power sources*. Newnes, 2013.
- [15] Knauth, Philippe. "Inorganic solid Li ion conductors: An overview." *Solid State Ionics* 180, no. 14-16 (2009): 911-916.
- [16] Li, Yutao, Weidong Zhou, Sen Xin, Shuai Li, Jinlong Zhu, Xujie Lü, Zhiming Cui, Quanxi Jia, Jianshi Zhou, Yusheng Zhao, and John B. Goodenough "Fluorine-doped Antiperovskite electrolyte for all-solid-state lithium-ion batteries" *Angewandte Chemie International Edition* 55, no. 34 (2016): 9965-9968.
- [17] Aono, Hiromichi, Eisuke Sugimoto, Yoshihiko Sadaoka, Nobuhito Imanaka, and Gin-ya Adachi. "The electrical properties of ceramic electrolytes for LiM_xTi_{2-x}(PO₄)_{3+y}Li₂O, M= Ge, Sn, Hf, and Zr systems." *Journal of The Electrochemical Society* 140, no. 7 (1993): 1827-1833.
- [18] Ortiz, Gregorio F., María C. López, Pedro Lavela, Candela Vidal-Abarca, and José L.

- Tirado. "Improved lithium-ion transport in NASICON-type lithium titanium phosphate by calcium and iron doping." *Solid State Ionics* 262 (2014): 573-577.
- [19] Norhaniza, R., R. H. Y. Subban, and N. S. Mohamed. "Cr and V substituted $\text{LiSn}_2\text{P}_3\text{O}_{12}$ solid electrolyte materials." *Journal of power sources* 244 (2013): 300-305.
- [20] Cao, Can, Zhuo-Bin Li, Xiao-Liang Wang, Xin-Bing Zhao, and Wei-Qiang Han. "Recent advances in inorganic solid electrolytes for lithium batteries." *Frontiers in Energy Research* 2 (2014): 25.
- [21] Hartmann, Pascal, Thomas Leichtweiss, Martin R. Busche, Meike Schneider, Marisa Reich, Joachim Sann, Philipp Adelhelm, and Jürgen Janek. "Degradation of NASICON-type materials in contact with lithium metal: formation of mixed conducting interphases (MCI) on solid electrolytes." *The Journal of Physical Chemistry C* 117, no. 41 (2013): 21064-21074.
- [22] Wenzel, Sebastian, Thomas Leichtweiss, Dominik Krüger, Joachim Sann, and Jürgen Janek. "Interphase formation on lithium solid electrolytes—An in situ approach to study interfacial reactions by photoelectron spectroscopy." *Solid State Ionics* 278 (2015): 98-105.
- [23] Thangadurai, Venkataraman, Sumaletha Narayanan, and Dana Pinzaru. "Garnet-type solid-state fast Li ion conductors for Li batteries: critical review." *Chemical Society Reviews* 43, no. 13 (2014): 4714-4727.
- [24] Cussen, Edmund J. "Structure and ionic conductivity in lithium garnets." *Journal of Materials Chemistry* 20, no. 25 (2010): 5167-5173.
- [25] Ramakumar, S., L. Satyanarayana, Sunkara V. Manorama, and Ramaswamy Murugan. "Structure and Li^+ dynamics of Sb-doped $\text{Li}_7\text{La}_3\text{Zr}_2\text{O}_{12}$ fast lithium ion conductors." *Physical Chemistry Chemical Physics* 15, no. 27 (2013): 11327-11338.
- [26] El Shinawi, Hany, and Jürgen Janek. "Stabilization of cubic lithium-stuffed garnets of the type " $\text{Li}_7\text{La}_3\text{Zr}_2\text{O}_{12}$ " by addition of gallium." *Journal of power sources* 225 (2013): 13-19.

- [27] Kim, Ki Hyun, Yasutoshi Iriyama, Kazuo Yamamoto, Shota Kumazaki, Toru Asaka, Kinuka Tanabe, Craig AJ Fisher, Tsukasa Hirayama, Ramaswamy Murugan, and Zempachi Ogumi. "Characterization of the interface between LiCoO_2 and $\text{Li}_7\text{La}_3\text{Zr}_2\text{O}_{12}$ in an all-solid-state rechargeable lithium battery." *Journal of Power Sources* 196, no. 2 (2011): 764-767.
- [28] West, A. R. "Crystal chemistry of some tetrahedral oxides." *Zeitschrift für Kristallographie-Crystalline Materials* 141, no. 1-6 (1975): 422-436.
- [29] Bron, Philipp, Sebastian Johansson, Klaus Zick, Jörn Schmedt auf der Günne, Stefanie Dehnen, and Bernhard Roling. " $\text{Li}_{10}\text{SnP}_2\text{S}_{12}$: an affordable lithium superionic conductor." *Journal of the American Chemical Society* 135, no. 42 (2013): 15694-15697.
- [30] Kamaya, Noriaki, Kenji Homma, Yuichiro Yamakawa, Masaaki Hirayama, Ryoji Kanno, Masao Yonemura, Takashi Kamiyama et al. "A lithium superionic conductor." *Nature materials* 10, no. 9 (2011): 682-686.
- [31] Kuhn, Alexander, Oliver Gerbig, Changbao Zhu, Frank Falkenberg, Joachim Maier, and Bettina V. Lotsch. "A new ultrafast superionic Li-conductor: ion dynamics in $\text{Li}_{11}\text{Si}_2\text{PS}_{12}$ and comparison with other tetragonal LGPS-type electrolytes." *Physical Chemistry Chemical Physics* 16, no. 28 (2014): 14669-14674.
- [32] Murayama, Masahiro, Ryoji Kanno, Michihiko Irie, Shinya Ito, Takayuki Hata, Noriyuki Sonoyama, and Yoji Kawamoto. "Synthesis of new lithium ionic conductor thio-LISICON—lithium silicon sulfides system." *Journal of Solid State Chemistry* 168, no. 1 (2002): 140-148.
- [33] Muramatsu, Hiromasa, Akitoshi Hayashi, Takamasa Ohtomo, Sigenori Hama, and Masahiro Tatsumisago "Structural change of $\text{Li}_2\text{S}-\text{P}_2\text{S}_5$ sulfide solid electrolytes in the atmosphere" *Solid State Ionics* 182, no. 1 (2011): 116-119.
- [34] Ohtomo, Takamasa, Akitoshi Hayashi, Masahiro Tatsumisago, and Koji Kawamoto "Suppression of H_2S gas generation from the $75\text{Li}_2\text{S}\cdot 25\text{P}_2\text{S}_5$ glass electrolyte by additives" *Journal of Materials Science* 48, no. 11 (2013): 4137-4142.

- [35] Tatsumisago, Masahiro, and Akitoshi Hayashi "Sulfide Glass-Ceramic Electrolytes for All Solid-State Lithium and Sodium Batteries" *International Journal of Applied Glass Science* 5, no. 3 (2014): 226-235.
- [36] Liu, D., W. Zhu, Z. Feng, A. Guerfi, A. Vijh, and K. Zaghib "Recent progress in sulfide-based solid electrolytes for Li-ion batteries" *Materials Science and Engineering: B* 213 (2016): 169-176.
- [37] Che, Haiying, Suli Chen, Yingying Xie, Hong Wang, Khalil Amine, Xiao-Zhen Liao, and Zi-Feng Ma "Electrolyte design strategies and research progress for room-temperature sodium-ion batteries" *Energy & Environmental Science* 10, no.5 (2017): 1075-1101.
- [38] Chen, Long, Yutao Li, Shuai-Peng Li, Li-Zhen Fan, Ce-Wen Nan, and John B. Goodenough "PEO/garnet composite electrolytes for solid-state lithium batteries: from "ceramic-in-polymer" to "polymer-in-ceramic"" *Nano Energy* 46 (2018): 176-184.
- [39] Owejan, Jeanette E., Jon P. Owejan, Steven C. DeCaluwe, and Joseph A. Dura "Solid electrolyte interphase in Li-ion batteries: evolving structures measured in situ by neutron reflectometry" *Chemistry of Materials* 24, no. 11 (2012): 2133-2140.
- [40] Tan, Guoqiang, Feng Wu, Chun Zhan, Jing Wang, Daobin Mu, Jun Lu, and Khalil Amine "Solid-state li-ion batteries using fast, stable, glassy nanocomposite electrolytes for good safety and long cycle-life" *Nano Letters* 16, no. 3 (2016): 1960-1968.
- [41] Mo, Shanshan, Penghao Lu, Fei Ding, Zhibin Xu, Jiaquan Liu, Xingjiang Liu, and Qiang Xu "High-temperature performance of all-solid-state battery assembled with 95 (0.7 Li₂S-0.3 P₂S₅)-5Li₃PO₄ glass electrolyte" *Solid State Ionics* 296 (2016): 37-41.
- [42] Ohtomo, Takamasa, Akitoshi Hayashi, Masahiro Tatsumisago, Yasushi Tsuchida, Shigenori Hama, and Koji Kawamoto "All-solid-state lithium secondary batteries using the 75Li₂S· 25P₂S₅ glass and the 70Li₂S· 30P₂S₅ glass-ceramic as solid electrolytes" *Journal of Power Sources* 233 (2013): 231-235.
- [43]] Lü, Xujie, John W. Howard, Aiping Chen, Jinlong Zhu, Shuai Li, Gang Wu, Paul

- Dowden, Hongwu Xu, Yusheng Zhao, and Quanxi Jia "Antiperovskite Li_3OCl Superior Ionic Conductor Films for Solid-State Li-Ion Batteries" *Advanced Science* 3, no. 3 (2016): 1500359.
- [44] Kanno, Ryoji, and Masahiro Murayama. "Lithium ionic conductor thio-LISICON: the $\text{Li}_2\text{S}-\text{GeS}_2-\text{P}_2\text{S}_5$ system." *Journal of the electrochemical society* 148, no. 7 (2001): A742-A746.
- [45] Rao, R. Prasada, and S. Adams. "Studies of lithium argyrodite solid electrolytes for all-solid-state batteries." *physica status solidi (a)* 208, no. 8 (2011): 1804-1807.
- [46] Mo, Yifei, Shyue Ping Ong, and Gerbrand Ceder. "First principles study of the $\text{Li}_{10}\text{GeP}_2\text{S}_{12}$ lithium super ionic conductor material." *Chemistry of Materials* 24, no. 1 (2012): 15-17.
- [47] Chung, Habin, and Byoungwoo Kang. "Increase in grain boundary ionic conductivity of $\text{Li}_{1-x}\text{Al}_x\text{Ge}_{1-x}\text{P}_2\text{S}_{12}$ by adding excess lithium." *Solid State Ionics* 263 (2014): 125-130.
- [48] Chi, E. O., W. S. Kim, and N. H. Hur. "Nearly zero temperature coefficient of resistivity in antiperovskite compound CuNMn_3 ." *Solid State Communications* 120, no. 7-8 (2001): 307-310.
- [49] Asano, K., K. Koyama, and K. Takenaka. "Magnetostriction in Mn_3CuN ." *Applied Physics Letters* 92, no. 16 (2008): 161909.
- [50] Tohei, T., Hirofumi Wada, and T. Kanomata. "Negative magnetocaloric effect at the antiferromagnetic to ferromagnetic transition of Mn_3GaC ." *Journal of Applied Physics* 94, no. 3 (2003): 1800-1802.
- [51] Kamishima, K., T. Goto, H. Nakagawa, N. Miura, M. Ohashi, N. Mori, T. Sasaki, and T. Kanomata. "Giant magnetoresistance in the intermetallic compound Mn_3GaC ." *Physical Review B* 63, no. 2 (2000), 63.2:024426.
- [52] He, T., Q. Huang, A. P. Ramirez, Y. Wang, K. A. Regan, and N. Rogado. "HMA, MK Haas, JS Slusky, K. Inumara, et al." *Nature* 411 (2001): 54-56.

- [53] Uehara, Masatomo, Akira Uehara, Katsuya Kozawa, and Yoshihide Kimishima. "New antiperovskite-type superconductor ZnN_yNi_3 ." *Journal of the Physical Society of Japan* 78, no. 3 (2009): 033702-033702.
- [54] Emly, Alexandra, Emmanouil Kioupakis, and Anton Van der Ven. "Phase stability and transport mechanisms in antiperovskite Li_3OCl and Li_3OBr superionic conductors." *Chemistry of Materials* 25, no. 23 (2013): 4663-4670.
- [55] Lu, Ziheng, Chi Chen, Zarah Medina Baiyee, Xin Chen, Chunming Niu, and Francesco Ciucci. "Defect chemistry and lithium transport in Li_3OCl anti-perovskite superionic conductors." *Physical Chemistry Chemical Physics* 17, no. 48 (2015): 32547-32555.
- [56] Li, Yutao, Weidong Zhou, Sen Xin, Shuai Li, Jinlong Zhu, Xujie Lü, Zhiming Cui, Quanxi Jia, Jianshi Zhou, Yusheng Zhao, and John B. Goodenough. "Fluorine-doped Antiperovskite electrolyte for all-solid-state lithium-ion batteries" *Angewandte Chemie International Edition* 55, no. 34 (2016): 9965-9968.
- [57] Emly, Alexandra, Emmanouil Kioupakis, and Anton Van der Ven. "Phase stability and transport mechanisms in antiperovskite Li_3OCl and Li_3OBr superionic conductors" *Chemistry of Materials* 25, no. 23 (2013): 4663-4670.
- [58] Lu, Ziheng, Chi Chen, Zarah Medina Baiyee, Xin Chen, Chunming Niu, and Francesco Ciucci. "Defect chemistry and lithium transport in Li_3OCl anti-perovskite superionic conductors" *Physical Chemistry Chemical Physics* 17, no. 48 (2015): 32547-32555.
- [59] Zhao, Yusheng, and Luke L. Daemen. "Superionic conductivity in lithium-rich antiperovskites" *Journal of the American Chemical Society* 134, no. 36 (2012): 15042-15047.
- [60] Zhang, Jianzhong, Jiantao Han, Jinlong Zhu, Zhijun Lin, Maria H. Braga, Luke L. Daemen, Liping Wang, and Yusheng Zhao. "High pressure-high temperature synthesis of lithium-rich Li_3O (Cl, Br) and $\text{Li}_{3-x}\text{Ca}_x/2\text{OCl}$ anti-perovskite halides" *Inorganic Chemistry Communications* 48 (2014): 140-143.
- [61] Li, Shuai, Jinlong Zhu, Yonggang Wang, John W. Howard, Xujie Lü, Yutao Li, Ravhi S.

- Kumar, Liping Wang, Luke L. Daemen, and Yusheng Zhao "Reaction mechanism studies towards effective fabrication of lithium-rich anti-perovskites Li₃OX (X= Cl, Br)" *Solid State Ionics* 284 (2016): 14-19.
- [62] Lü, Xujie, John W. Howard, Aiping Chen, Jinlong Zhu, Shuai Li, Gang Wu, Paul Dowden, Hongwu Xu, Yusheng Zhao, and Quanxi Jia "Antiperovskite Li₃OCl Superionic Conductor Films for Solid-State Li-Ion Batteries" *Advanced Science* 3, no. 3 (2016): 1500359.
- [63] Braga, M. H., Jorge Amaral Ferreira, V. Stockhausen, J. E. Oliveira, and A. El-Azab "Novel Li₃ClO based glasses with superionic properties for lithium batteries" *Journal of Materials Chemistry A* 2, no. 15 (2014): 5470-5480.
- [64] Lu, Ziheng, Chi Chen, Zarah Medina Baiyee, Xin Chen, Chunming Niu, and Francesco Ciucci. "Defect chemistry and lithium transport in Li₃OCl anti-perovskite superionic conductors." *Physical Chemistry Chemical Physics* 17, no. 48 (2015): 32547-32555
- [65] Li, Shuai, Jinlong Zhu, Yonggang Wang, John W. Howard, Xujie Lü, Yutao Li, Ravhi S. Kumar, Liping Wang, Luke L. Daemen, and Yusheng Zhao. "Reaction mechanism studies towards effective fabrication of lithium-rich anti-perovskites Li₃OX (X= Cl, Br)." *Solid State Ionics* 284 (2016): 14-19.
- [66] Lü, Xujie, John W. Howard, Aiping Chen, Jinlong Zhu, Shuai Li, Gang Wu, Paul Dowden, Hongwu Xu, Yusheng Zhao, and Quanxi Jia. "Antiperovskite Li₃OCl Superionic Conductor Films for Solid-State Li-Ion Batteries." *Advanced Science* 3, no. 3 (2016): 1500359.
- [67] Lü, Xujie, Gang Wu, John W. Howard, Aiping Chen, Yusheng Zhao, Luke L. Daemen, and Quanxi Jia. "Li-rich anti-perovskite Li₃OCl films with enhanced ionic conductivity." *Chemical Communications* 50, no. 78 (2014): 11520-11522.
- [68] Chen, S., Xie, D., Liu, G., Mwizerwa, J. P., Zhang, Q., Zhao, Y., ... & Yao, X. (2018). Sulfide solid electrolytes for all-solid-state lithium batteries: structure, conductivity, stability and application. *Energy Storage Materials*, 14, 58-74.

- [69] Sun, Y. Z., Huang, J. Q., Zhao, C. Z., & Zhang, Q. (2017). A review of solid electrolytes for safe lithium-sulfur batteries. *Science China Chemistry*, 60(12), 1508-1526.
- [70] Zheng, F., Kotobuki, M., Song, S., Lai, M. O., & Lu, L. (2018). Review on solid electrolytes for all-solid-state lithium-ion batteries. *Journal of Power Sources*, 389, 198-213..
- [71] Deiseroth, H. J., Kong, S. T., Eckert, H., Vannahme, J., Reiner, C., Zaiß, T., & Schlosser, M. (2008). Li₆PS₅X: a class of crystalline Li-rich solids with an unusually high Li⁺ mobility. *Angewandte Chemie*, 120(4), 767-770.

Chapter 2. General experimental

2-1. Physical characterization

2-1-1. X-ray diffraction (XRD)

X-ray powder diffraction (XRD) is an essential technique that uses the diffraction of X-rays on powder or microcrystalline samples for the study of crystal structures and those of volume. The most popular analysis method for structural changes by crystal structures and environments (atmosphere, temperature, etc.) of the powder samples. It is based on the constructive interference of a monochromatic X-ray and a crystalline sample. Therefore, it is possible to Figure out the shape of crystallines from the diffraction of a crystal in any direction, the structure of a material is also contained in the forward scattering. The inorganic powders were usually used as the sample for the diffraction analysis. The samples interacted with the incident X-ray beam as followed by Bragg's Law equation (Fig 2.1).

$$\text{Bragg equation : } n\lambda = 2d_{hkl}\sin\theta_{hkl} \quad (n=1, 2, 3 \dots) \quad (2.1)$$

Where λ is the frequency of the incident beam, d is d-spacing, θ is the diffraction angles when the samples interact with the incident beam, hkl is miller index. This law-related the wavelength of electromagnetic radiation to the diffraction angle and the lattice spacing in a crystalline powder. The difference in path length between reflections on neighboring planes is $d_{hkl} \sin\theta_{hkl}$. For example, the smaller the distance d-spacing, the larger the diffraction angle θ . When the wavelength λ increase, the diffraction angle θ increase. Because the difference of path length means the different interference between the diffraction wavelength, the angle is the main scale for determining the crystals. From the equations, the d-spacing can be calculated by considering Miller indices and unit cell parameters it was related to 7 types of crystal system. Figure 2.2 is the table of the crystal system and d-spacing [1, 2]. The crystals depend on three cell parameters (a, b, c) and three angles (α, β, γ). The crystals are different symmetries from the cubic crystal composed with three same parameter values and three 90 degrees angles to triclinic. According to the rotational symmetry, there are 14 different Bravais Lattices in which similar points can be arranged in a three-dimensional space not 28 cases by French crystallographer August Bravais in 1848. The 14 Bravais

Lattices are combined with 32-point group symmetries and finally, give the 230 space groups. This powerful analysis can be applied to almost inorganic materials which have quite electronic density except for low periodic number such as Li due to its low electronic density.

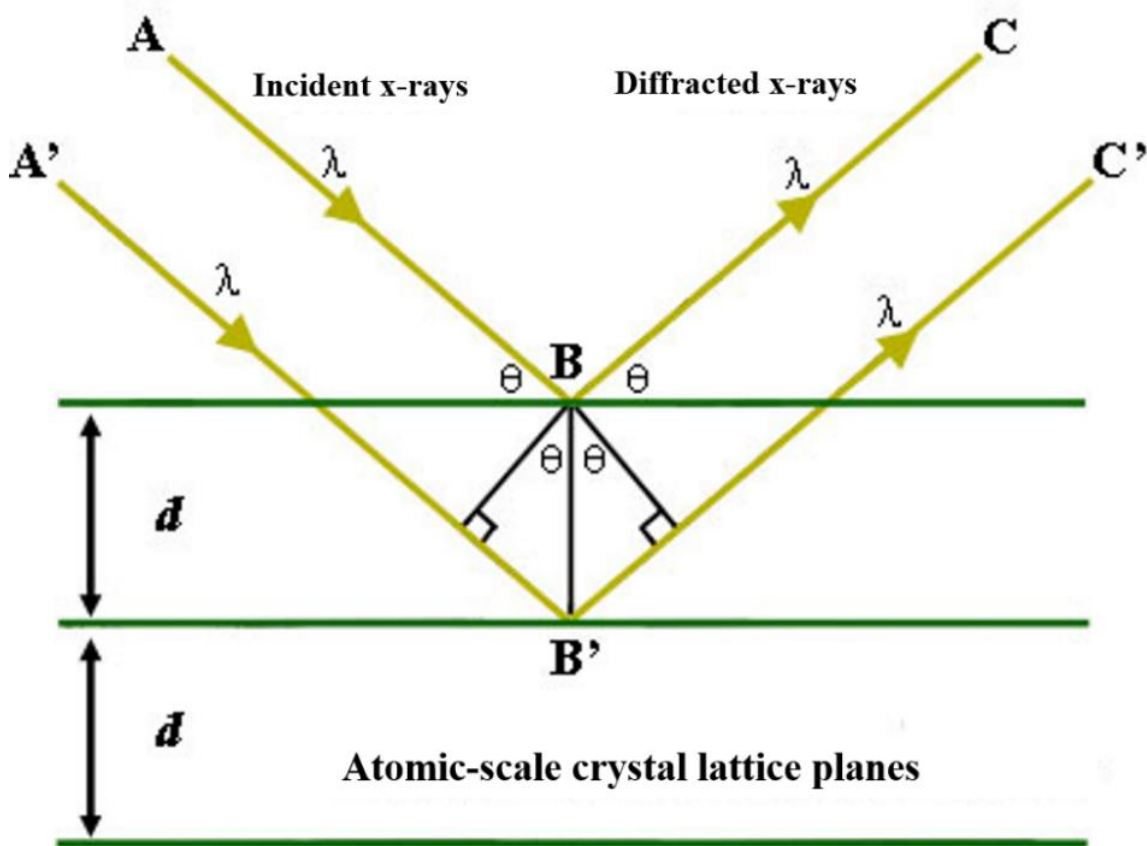


Figure 2.1 Bragg reflection on a set of atomic planes.

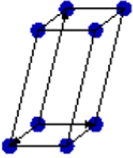
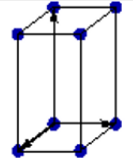
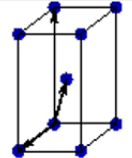
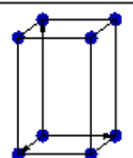
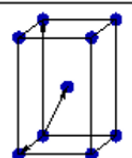
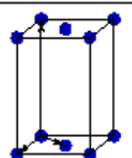
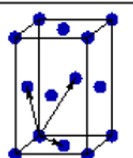
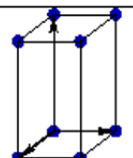
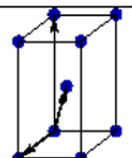
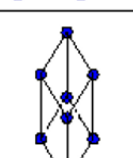
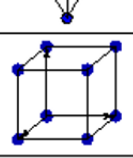
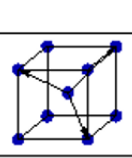
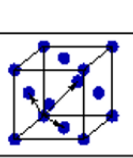
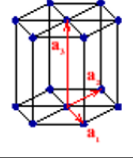
Bravais lattice	Parameters	Simple (P)	Volume centered (I)	Base centered (C)	Face centered (F)
Triclinic	$a_1 \neq a_2 \neq a_3$ $\alpha_{12} \neq \alpha_{23} \neq \alpha_{31}$				
Monoclinic	$a_1 \neq a_2 \neq a_3$ $\alpha_{23} = \alpha_{31} = 90^\circ$ $\alpha_{12} \neq 90^\circ$				
Orthorhombic	$a_1 \neq a_2 \neq a_3$ $\alpha_{12} = \alpha_{23} = \alpha_{31} = 90^\circ$				
Tetragonal	$a_1 = a_2 \neq a_3$ $\alpha_{12} = \alpha_{23} = \alpha_{31} = 90^\circ$				
Trigonal	$a_1 = a_2 = a_3$ $\alpha_{12} = \alpha_{23} = \alpha_{31} < 120^\circ$				
Cubic	$a_1 = a_2 = a_3$ $\alpha_{12} = \alpha_{23} = \alpha_{31} = 90^\circ$				
Hexagonal	$a_1 = a_2 \neq a_3$ $\alpha_{12} = 120^\circ$ $\alpha_{23} = \alpha_{31} = 90^\circ$				

Figure 2.2 Seven crystal system and 14 Bravais lattice.

2-1-2. Field emission scanning electron microscopy (FE-SEM)

FE-SEM is a Field Emission Scanning Electron Microscope that operates with a high-energy electron beam in a scan pattern instead of a light source. These electrons are released by a field emission source in a field emission gun. These electron emitters can produce up to 1000x the emission of a tungsten filament with a high vacuum atmosphere to prevent unnecessary interaction between gas molecules and the electron beam. After the electrons

beam exit the electron gun, a monochromatic beam uses metal apertures and magnetic lenses. And Finally, the detectors of each type of electrons are placed in the microscopes that collect signals to produce an image of the patterns [3]. The electrons from the primary beam spread out in the sample to form the interaction volume. The size of the interaction volume depends on the accelerating voltage value of the primary electron beam and the atomic number of the sample. The interaction volume increase with a larger accelerating voltage, but smaller for samples with a higher atomic number. Secondary electrons are produced from the surface of the sample or topmost part of the interaction volume and X-rays are generated within the whole of the interaction volume [4]. FE-SEM is used to visualized information of the local areas on the surface of chemicals. Also, the analysis can be combined with Energy-dispersive X-ray spectroscopy (EDS) for good elemental analysis such as elemental composition near the surface of the samples with atomic number (Z) >3 . The combination can also visualize the element distribution in a sample by mapping which showing the concentration of one element over a selected area of images of the sample. SEM-EDS mapping analysis is an effective elemental mapping that showing how to concentrate one element varies over an area of images of material.

2-1-3. Laser Raman spectroscopy

Raman spectroscopy is a spectroscopic technique typically used to determine vibrational modes of molecules, although rotational and other low-frequency modes of systems may also be observed. Raman spectroscopy is commonly used in chemistry to provide a structural fingerprint by which molecules can be identified. The light source used in Raman spectroscopy is a laser. The laser light is used because it is a very intense beam of nearly monochromatic light that can interact with sample molecules. When the radiation is absorbed, a molecule jumps to a higher vibrational or rotational energy level. Raman spectroscopy relies upon the inelastic scattering of photons, known as Raman scattering. A source of monochromatic light, usually from a laser in the visible, near-infrared, or near ultraviolet range is used, although X-rays can also be used. The laser light interacts with molecular vibrations, phonons, or other excitations in the system, resulting in the energy of the laser photons being shifted up or down. The energy shift gives information about the vibrational modes in the system. Infrared spectroscopy typically yields similar, complementary,

information. That's why we can detect the structure of material using an excitation wavelength.

2-2. Electrochemical analysis

2-2-1. Electrochemical impedance spectroscopy (EIS)

Electrochemical impedance spectroscopy (EIS) is a powerful technique to measure the electrical impedance resistance of an electrode or a whole-cell system. The impedance of an electrochemical system is defined as the resistance when an AC voltage or current is applied over a range of frequencies. The current-voltage relationship of the impedance can be expressed as a followed equation.

$$Z(w) = \frac{V(t)}{I(t)} = \frac{V_m \sin(wt)}{I_m \sin(wt-\theta)} = Z \exp(j\theta) \quad (2.2)$$

Where $v(t)$ and $I(t)$ are AC voltage and current, $Z(w)$ is impedance, w is frequency ($w=2\pi f$). The equation is derived by Euler's rule as below:

$$Z(w) = Z_{re} + iZ_{im} \quad (2.3)$$

Where Z_{re} and Z_{im} are the real and imaginary parts of the impedance in the Nyquist plot which is one of the methods for expressing impedance like Figure 2.3. From the obtained result, an equivalent circuit is deduced and is proved by the fitting procedure. The equivalent circuit gives the resistance component. For example, the real impedance value on the x-axis from the O to the initial value is mass transfer resistance considered as electrolyte resistance, the real value of the diameter of the semicircle is charge transfer resistance related to a surface area of an electrode, and the Warburg region which is the tail is Warburg impedance related with a lithium diffusion coefficient of active material.

In the case of the solid electrolyte, the way to interpret the equivalent circuit is different. Figure 8 shows a suitable example for an equivalent circuit of a solid electrolyte. The real value from 0 to the first semicircle means bulk resistance by a crystal structure and the insufficient contact between the particles of an active material and a solid electrolyte material. The second semicircle is the resistance by the grain boundary meaning a crack of solid electrolyte pellet. These factors are the main resistance by solid electrolytes. The ionic conductivity of the solid electrolyte is calculated by the below equation.

$$\sigma = \frac{l}{RA} = S/cm \quad (2.4)$$

Where l is thickness of a solid electrolyte pellet, R is the resistance, and A is the area of the pellet.

2-2-2. Cyclic voltammetry

Cyclic voltammetry is a typical technique that the current flow can be measured by controlling the potential of the working electrode. This method is a principle of observing the change of current while applying a voltage at a constant scan rate (mV/s). This electrochemical analysis provides much information such as the oxidation and reduction mechanism of a material, reversibility from the voltage gap of oxidation and reduction, and reactivity from the area of current x voltage [4-6]. The measurement can also calculate the diffusion coefficient of lithium ions diffused into an active material through a current change that varies with the scan rate [7, 8].

When the cyclic voltammetry is applied to solid electrolytes, its purpose is to evaluate the electrochemical stability of solid electrolyte [9, 10]. The configuration of the cell for the cyclic voltammetry is mainly composed of symmetric Li/electrolyte/SUS or Cu (reference/working/counter electrodes) [9]. The stability of the solid electrolyte is evaluated by comparing the current change while the voltage is being scanned at a constant rate. This method is not accurate for comparing the degree of reaction of the solid electrolytes but is good at observing the reaction voltage of the electrolytes.

2-2-3. Direct current cycling (DC-cycling)

DC-cycling measurement is one of the galvanostatic measurements such as galvanostatic charge-discharge and galvanostatic intermittent titration technique. The simple electrochemical analysis is conducted by applying the constant current to a cell during charge and discharge with time cut off condition. Recently, this measurement has been used to evaluate the electrochemical stability of solid electrolyte materials (versus Li metal Li/SE/Li) [10]. Compare with cyclic voltammetry, DC-cycling is good for comparing electrochemical reactivity as well as the resistance of solid electrolytes. The example of DC-cycling is in Figure 1.12 [10]. When the solid electrolyte reacts with the lithium metal, the voltage of the

cell changes in an increasing direction. The reason for increasing voltage is the resistance by SEI formation. As followed by the simple ohm's law ($V=IR$), the voltage increases by some resistance factor when the constant current (mA/cm^2) is applied. Because other conditions are the same, the resistance is considered by SEI formation between solid electrolyte and Li metal like Li/SEI/SE. Conversely, when the voltage is maintained at a constant value, the solid electrolyte material is considered stable with Li metal. The electrolyte may not react with Li metal or form the SEI at a very slow rate. In other cases, the solid electrolyte reacts with Li metal at initial cycles and formed stable SEI. Therefore, the voltage changes do not occur after the first few cycles. This analysis is simple but gives much information about the electrochemical stability of a material.

2-2-4. Galvanostatic charge-discharge measurements (CD)

During the galvanostatic cycling of batteries, the charge and discharge currents are often expressed as a C-rate which is a measure of the rate. A C-rate of 1 C means that the necessary current is applied or drained from the battery to completely charge or discharge it in 1 hour. Since the capacity is expressed in ampere per hour,

0. calculating the current necessary to charge or discharge a battery is straightforward.

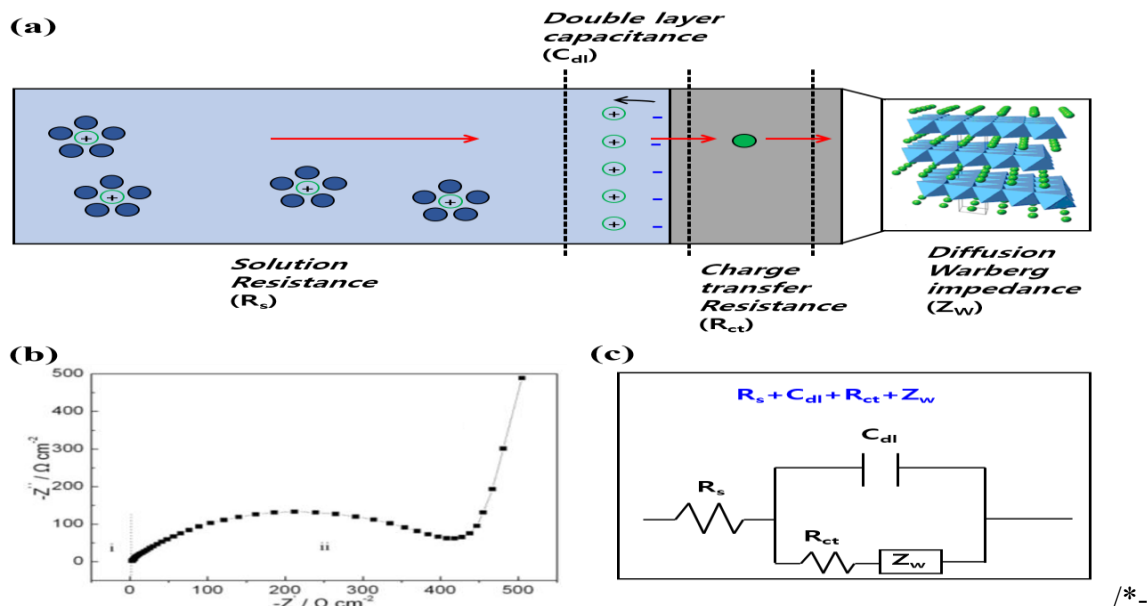


Figure 2.3 (a) The Li^+ diffusion mechanism of lithium ion batteries, (b) Nyquist plot of an electrode, and (c) equivalent circuit from the Nyquist plot

Reference

- [1] Pope, Christopher G. "X-ray diffraction and the Bragg equation." *Journal of chemical education* 74, no. 1 (1997): 74.1:129.
- [2] Hammond, Christopher, and Christopher Hammond. *The basics of crystallography and diffraction*. Vol. 214. Oxford, 2001.
- [3] Sheng, Lee Hwang. "Nanostructured Phosphate-based Electrode Materials for Lithium Batteries." PhD diss., 2012.
- [4] Gosser, David K. *Cyclic voltammetry: simulation and analysis of reaction mechanisms*. Vol. 43. New York: VCH, 1993.
- [5] Kounaves, Samuel P. "Voltammetric techniques." *Handbook of instrumental techniques for analytical chemistry* (1997): 709-726.
- [6] Sheng, Lee Hwang. "Nanostructured Phosphate-based Electrode Materials for Lithium Batteries." PhD diss., 2012.
- [7] Tang, S. B., M. O. Lai, and L. Lu. "Li-ion diffusion in highly (0 0 3) oriented LiCoO₂ thin film cathode prepared by pulsed laser deposition." *Journal of Alloys and Compounds* 449, no. 1-2 (2008): 300-303.
- [8] Wen, C. John, B. A. Boukamp, Robert A. Huggins, and W. Weppner. "Thermodynamic and mass transport properties of "LiAl". " *Journal of The Electrochemical Society* 126, no. 12 (1979): 2258-2266.
- [9] Neudecker, B. J., and W. Weppner. "Li₉SiAlO₈: A lithium ion electrolyte for voltages above 5.4 V." *Journal of the electrochemical society* 143, no. 7 (1996): 2198-2203.
- [10] Hood, Zachary D., Hui Wang, Amaresh Samuthira Pandian, Jong Kahk Keum, and Chengdu Liang. "Li₂OHCl crystalline electrolyte for stable metallic lithium anodes." *Journal of the American Chemical Society* 138, no. 6 (2016): 1768-1771.

Chapter 3. Electrochemical performance of the mixed solid electrolyte $(100-x)\text{Li}_3\text{SI-xLi}_6\text{PS}_5\text{Cl}$ ($x=0, 10, 20$ and 30) for all solid state lithium batteries

3-1. Introduction

Battery technology for chemical energy storage, such as lead-acid batteries, nickel system batteries, and lithium-ion batteries (LiBs), is considered to be the most promising energy storage technologies in the industry. In particular, LiBs are preferred and used in many electronic devices due to its compactness, high energy and power density, and long cycle life[1]. However, the organic electrolyte in LiBs has a large side reaction with the electrode and there is a risk of fire due to external shock or heat[2]. Also, known non-aqueous electrolytes used in LiBs are thermodynamically unstable over a wide voltage window[3][4]. To solve the shortcomings of such liquid electrolytes, solid electrolytes with higher electrochemical stability and high durability are attracting attention[5][6]. However, when we use solid electrolytes, compared to a liquid electrolytes, ionic conductivity is low at room temperature, so resistance between electrode and electrolyte is high, and cycle stability is low[5][6]. In addition, there is a problem of volume expansion due to the formation of a lithium dendrite due to chemical instability between the lithium metal and the solid electrolyte.[7][8].

To solve this problem, solid electrolytes of various materials have been developed, but it is not easy to apply them to all solid batteries due to problems with each material. These problems can also be found in representative solid electrolytic materials such as sulfide-based SE and oxide-based SE. Sulfide-based solid electrolytes have relatively high ionic conductivity but produce unstable and toxic H_2S gases in the atmosphere. Also, due to side reactions with lithium metal, dendrite composed of Li_2S and Li_3P is formed[9][10]. Oxide-

based solid electrolytes are chemically stable in the atmosphere but have low ionic conductivity[10][11]. Accordingly, recent efforts have been made to synthesize mixed solid electrolytes and apply them to ASSLBs in order to reduce the disadvantages of each material and maximize the advantages[12][13][14][15][16][17][18]. For example, in Tatsumisago et al group, Li_3PS_4 and LiBH_4 were mixed to increase the stability with lithium metal and synthesized a solid electrolyte that improved lithium ion conductivity[12]. In the Xu et al group, $\text{Li}_7\text{P}_3\text{S}_{11}$ was doped with LiPO_4 to reduce side reactions between the cathode and the solid electrolyte and the lithium ion conductivity was improved[13].

Inspired by the above research, we are inspired by the experiment above to synthesize a mixed solid electrolyte. One of the materials we have chosen is anti-perovskite material. Li_3OCl is the most well-known anti-perovskite solid electrolyte. It has excellent stability with lithium metal and has superionic lithium-ion conductivity and low electrical conductivity. Besides, it has the advantage that the activation energy barrier required for ion transfer through three-dimensional conduction is low[19]. However, it decomposes into Li_2O and LiCl at operating temperature, and Li_2O has low ionic conductivity, which is not good for lithium diffusion[20]. Therefore, attention has been paid to substances that replace O in Li_3OCl with S[21]. We applied Li_3SI to the mixed solid electrolyte, which has a relatively lower tolerance coefficient $t=0.81$ than the ordered structure of Li_3OCl ($t=0.85$), which provides greater ionic mobility[22][23]. Li_3SI forms Anti-perovskite with a structure with BCC anion packing through the phase transition between Li_2S and LiI . Since the S^{2-} and I bcc anion packing of lithium sulfide is difficult to synthesize because of its low stability, a method of increasing the synthesis temperature has been proposed as a solution to this problem[21][22].

However, as a result of synthesis at various temperatures, the material synthesized at room temperature had the highest ionic conductivity, and the XRD results all showed the same pattern. We predicted these substances as anti-perovskite Li_3SI and conducted experiments. The other material for mixed solid electrolyte synthesis is the argyrodite material. Argyrodites are a type of chalcogenide structure s containing fast cation Ag^+ or Cu^+ in the form of $\text{Ag}_6\text{PS}_5\text{X}$ or $\text{Cu}_6\text{PS}_5\text{X}$ [24][25][26][27][28][29]. Recently, Deiseroth et al synthesized Li + argyrodite by converting Cu or Ag cation to lithium. The synthesized Li +

argyrodite has a very high ionic conductivity[30]. $\text{Li}_6\text{PS}_5\text{X}$ ($\text{X} = \text{Cl}, \text{Br}, \text{I}$) is an argyrodite structure in which Li is removed from Li_7PS_6 and S is replaced by an additional element, with a very high ionic conductivity at room temperature ($10^{-2} \sim 10^{-3} \text{S/cm}$) due to the soft lattice shape[9][31]. As shown on the structure of $\text{Li}_6\text{PS}_5\text{X}$, four of the 136 tetrahedral holes formed by P and S atoms in the unit cell are structures in which the PS_4 tetrahedron does not share a common S atom, and the remaining 132 tetrahedral holes are partially occupied disorderly by Li^+ . Due to this disorder, the movement of lithium becomes smooth and, accordingly, high lithium-ion conductivity[30][32]. But, $\text{Li}_6\text{PS}_5\text{I}$ has a structure aligned with the large ionic radius of iodine, so it has low ionic conductivity, and $\text{Li}_6\text{PS}_5\text{Cl}$ containing the smallest halogen element has the highest ionic conductivity[33].

However, despite the very high ionic conductivity of $\text{Li}_6\text{PS}_5\text{Cl}$, side reactions occur frequently at the interface between the electrode and the electrolyte, and it is particularly unstable when Li metal is used as an anode. Due to this effect, the cycle stability of the battery and capacity decreases[34][35][36][37].

The synthesis of a solid electrolyte of $(100-x)\text{Li}_3\text{SI}-x\text{Li}_6\text{PS}_5\text{Cl}$ ($x = 0, 10, 20, \text{ and } 30$) resulted in better solid electrolyte performance than when Li_3SI and $\text{Li}_6\text{PS}_5\text{Cl}$ were each single electrolyte. The mixed $(100-x)\text{Li}_3\text{SI}-x\text{Li}_6\text{PS}_5\text{Cl}$ ($x = 0, 10, 20, \text{ and } 30$) solid electrolyte improved the stability of lithium metal compared to Li_3SI and $\text{Li}_6\text{PS}_5\text{Cl}$ electrolytes, and improved battery capacity and cycle stability when applied to ASSLBs.

3-2. Experimental

Argyrodite $\text{Li}_6\text{PS}_5\text{Cl}$ mixes Li_2S (99.98%, Sigma-Aldrich), P_2S_5 (99%, Sigma-Aldrich), and LiCl ($\geq 99.98\%$, Sigma-Aldrich) stoichiometrically at 5:1:2 in a glove box in an Ar atmosphere. The well-mixed sample is synthesized by a mechanical dry milling process with 10mm ZrO_2 balls (79g) at 400 rpm for 15 hours. The synthesized $\text{Li}_6\text{PS}_5\text{Cl}$ was crystallized by sintering at 550 °C (heating rate: 2 °C/min) for 10 hours at Ar atmosphere. Anti-perovskite Li_3SI is synthesized by a mechanical dry milling process with 10mm ZrO_2 balls (79g) at 400rpm for 24 hours after mixing Li_2S (99.98%, Sigma-Aldrich) and LiI (99% \geq , Sigma-Aldrich) stoichiometrically at 1:1 in a glove box in an Ar environment. The synthesized $\text{Li}_6\text{PS}_5\text{Cl}$ and

Li₃SI were mixed well in a glove box in an Ar atmosphere according to their respective molar ratios and then performed to a mechanical dry milling process with 10mm ZrO₂ balls (79g) at 400rpm for 12 hours.

XRD (X-Ray Diffraction) measurements were performed by applying Cu-K α radiation ($\lambda = 1.5418 \text{ \AA}$) using an X-ray diffractometer (Rigaku-Ultima (IV)). At a step size of 0.01° , the crystallinity of the powder was measured in the 2θ range of 10 to 80° . Field emission scanning electron microscopy (FE-SEM) images were measured using JEOL, JSM-7610F with an accelerating voltage of 15 kV to confirm the elemental distribution in solid electrolyte samples.

To measure the ionic conductivity and calculate the activation energy of the electrolyte, electrochemical impedance spectroscopy (EIS) analysis was performed in the frequency range of 7 MHz to 1 Hz with an amplitude of 50 mV using an SP-300 analyzer. The measurements were made using In/SE/In symmetric cells. For this measurement, 0.25 g (thickness: 2 mm) solid electrolyte was compressed at 300 bar using a 10 mm diameter mold. The indium foils used for the EIS measurement were 50 μ m thick foil made by Nilaco. Cyclic voltammetry was measured with SUS(stainless steel)/SE/Li cells of solid electrolyte with a scan rate of 1 mV/s in a voltage window of -0.5 V to 5 V at room temperature using WonATech. Electrolyte pellets were compressed at 300 bar to make pellets, then lithium foil and SUS plates were placed on both sides of the pellets and compressed together at 30 bar. DC-cycling was measured by applying a constant direct current of 1.0 mA cm^{-2} to a Li/SE/Li symmetric cell for 100 hours at room temperature using WonATech. Cathode composite was made by mixing Li(Ni_{0.8}Co_{0.1}Mn_{0.1})O₂ called NCM811 and Li₆PS₅Cl solid electrolyte, Super P in a ratio of 70:28:2. To make cathode composite uniform, the 300 bar compression and the grinding process were repeated 3 times. As the anode, Li-In alloy was used to prevent instability between lithium metal and solid electrolyte. Li-In alloy was made by mixing lithium and indium powders for 3 times using mixer in a ratio of Li:In=1:2.0.2g solid electrolyte was compressed at 300bar using a 16mm diameter mold, and a positive electrode mixture and Li-In alloy were added to each side of the solid electrolyte and then compressed again to 300bar to produce a cell. Li-In alloy/SE/Li(Ni_{0.8}Co_{0.1}Mn_{0.1})O₂ cells were performed to charge galvanostatic cycle measurements in the range of 2.00 to 3.80V at a current density

of 0.1C (23.8mA/ g) using WonATech.

3-3. Results and discussion

3-3-1. Characterization

Figure.1 shows the XRD diffraction patterns of solid electrolyte $(100-x)\text{Li}_3\text{SI}-x\text{Li}_6\text{PS}_5\text{Cl}$ mixed through a ball-mill process. As the mixing ratio of $\text{Li}_6\text{PS}_5\text{Cl}$ increases, the XRD diffraction patterns appear amorphous. This reason can be seen in figure.2 After going through the ball-mill process in the synthesis process, the $\text{Li}_6\text{PS}_5\text{Cl}$ samples crystallized through the annealing process are mixed with Li_3SI and molar ratio and then go through the ball-mill process again. In this process, $\text{Li}_6\text{PS}_5\text{Cl}$ is not completely formed, leaving unconsumed Li_2S . Accordingly, it is shown that as the amount of $\text{Li}_6\text{PS}_5\text{Cl}$ increases, the intensity of the XRD diffraction peak of Li_2S increases at 27° and the intensity of the main diffraction peak of Li_3SI decreases at 26° . The main diffraction patterns of Li_3SI at 25° , 26° , 29° , 42° , 44° , 50° , and 52° indicate anti-perovskite structure. $\text{Li}_6\text{PS}_5\text{Cl}$ exhibits major XRD diffraction patterns at 15° , 17° , 25° , 29° , 31° , 39° , 45° , 47° , and 52° indicating an argyrodite structure[36]. The diffraction pattern of $90\text{Li}_3\text{SI}-10\text{Li}_6\text{PS}_5\text{Cl}$ shows that the main peak intensity of Li_3SI decreases at 25° , and the diffraction patterns of $\text{Li}_6\text{PS}_5\text{Cl}$ are not confirmed. However, XRD of $80\text{Li}_3\text{SI}-20\text{Li}_6\text{PS}_5\text{Cl}$, the diffraction pattern of $\text{Li}_6\text{PS}_5\text{Cl}$ indicate at 15° , 30° , and 44° , and the diffraction pattern of Li_2S not consumed at 26° is shown. The XRD of $70\text{Li}_3\text{SI}-30\text{Li}_6\text{PS}_5\text{Cl}$ shows the main diffraction patterns of $\text{Li}_6\text{PS}_5\text{Cl}$ at 15° , 28° , 30° , 44° , and 52° . Besides, the intensity of the diffraction pattern of Li_2S that was not consumed is also increased. As the mixing ratio of $\text{Li}_6\text{PS}_5\text{Cl}$ increases, the diffraction pattern of $\text{Li}_6\text{PS}_5\text{Cl}$ increases in the diffraction pattern of the mixed solid electrolyte, confirming that mixing is well performed. Besides, the peak intensity of the Li_2S diffraction pattern that is not consumed to form $\text{Li}_6\text{PS}_5\text{Cl}$ tends to increase. As unconsumed Li_2S increases, SEI layers of Li_2S and Li_2S_2 are formed on the lithium metal, causing a side reaction that changes the characteristics of the electrode[38]. For this reason, it is shown in figure.4 that when the mixing ratio of $\text{Li}_6\text{PS}_5\text{Cl}$ exceeds 30, the width of the increase in ion conductivity decreases. Also, in figure.8, it can be seen that the performance of the ASSLB battery is also reduced at

70Li₃SI-30Li₆PS₅Cl.

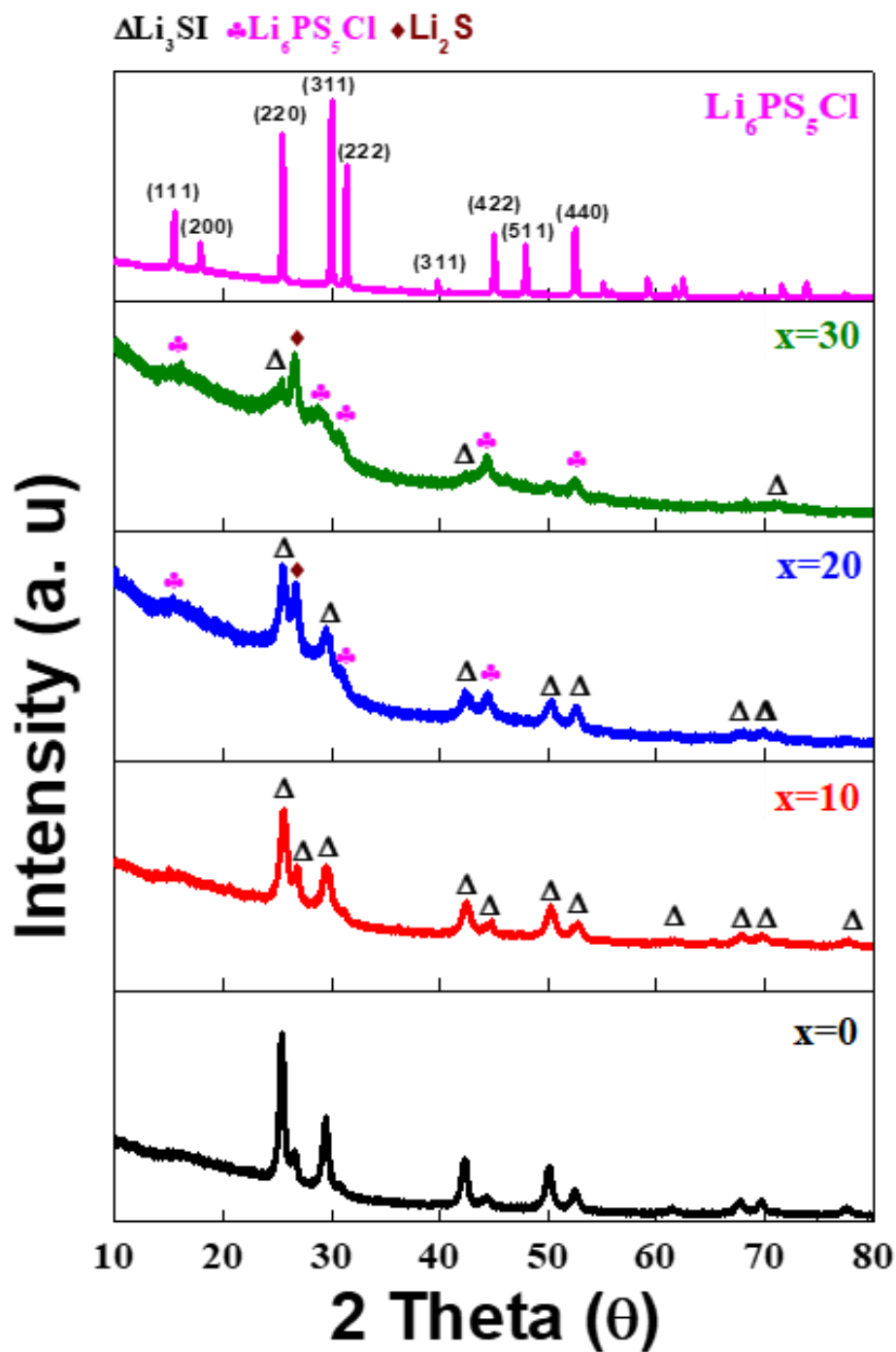


Figure. 3.1. XRD for (100-x)Li₃SI -xLi₆PS₅Cl (x = 0, 10, 20, and 30).

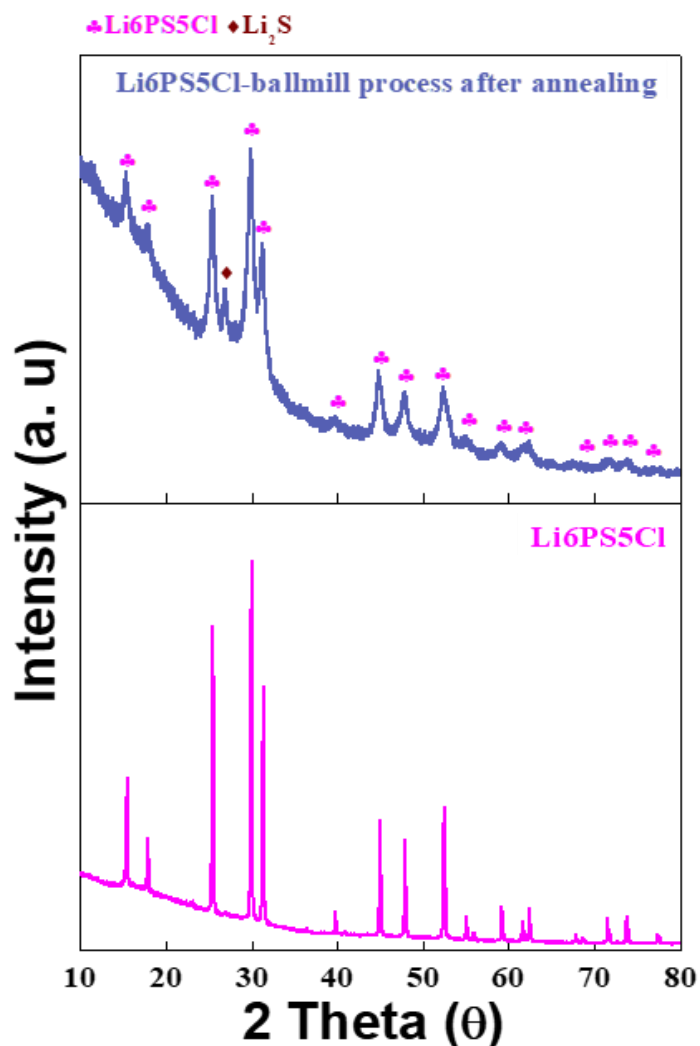


Figure. 3.2. XRD comparison of $\text{Li}_6\text{PS}_5\text{Cl}$ and $\text{Li}_6\text{PS}_5\text{Cl}$ -ballmill process after annealing.

SEM measurements were performed to observe the morphology of the mixed solid electrolyte $(100-x)\text{Li}_3\text{SI}-x\text{Li}_6\text{PS}_5\text{Cl}$. Figure.3 shows SEM images of mixed solid electrolytes. Li_3SI synthesized by mechanical milling method has a non-uniform particle size of $1\mu\text{m} < < 10\mu\text{m}$. $\text{Li}_6\text{PS}_5\text{Cl}$ has a more non-uniform particle size and has a size of $1\mu\text{m} < < 20\mu\text{m}$. The mixed solid electrolytes have similarly very non-uniform particle size, and as $\text{Li}_6\text{PS}_5\text{Cl}$ is added, agglomeration is observed. These results are similar to the phenomenon of changing to the amorphous diffraction pattern seen in XRD. We believe that this phenomenon is caused by Li_2S , which is not consumed, and $\text{Li}_6\text{PS}_5\text{Cl}$, which is formed amorphous by it.

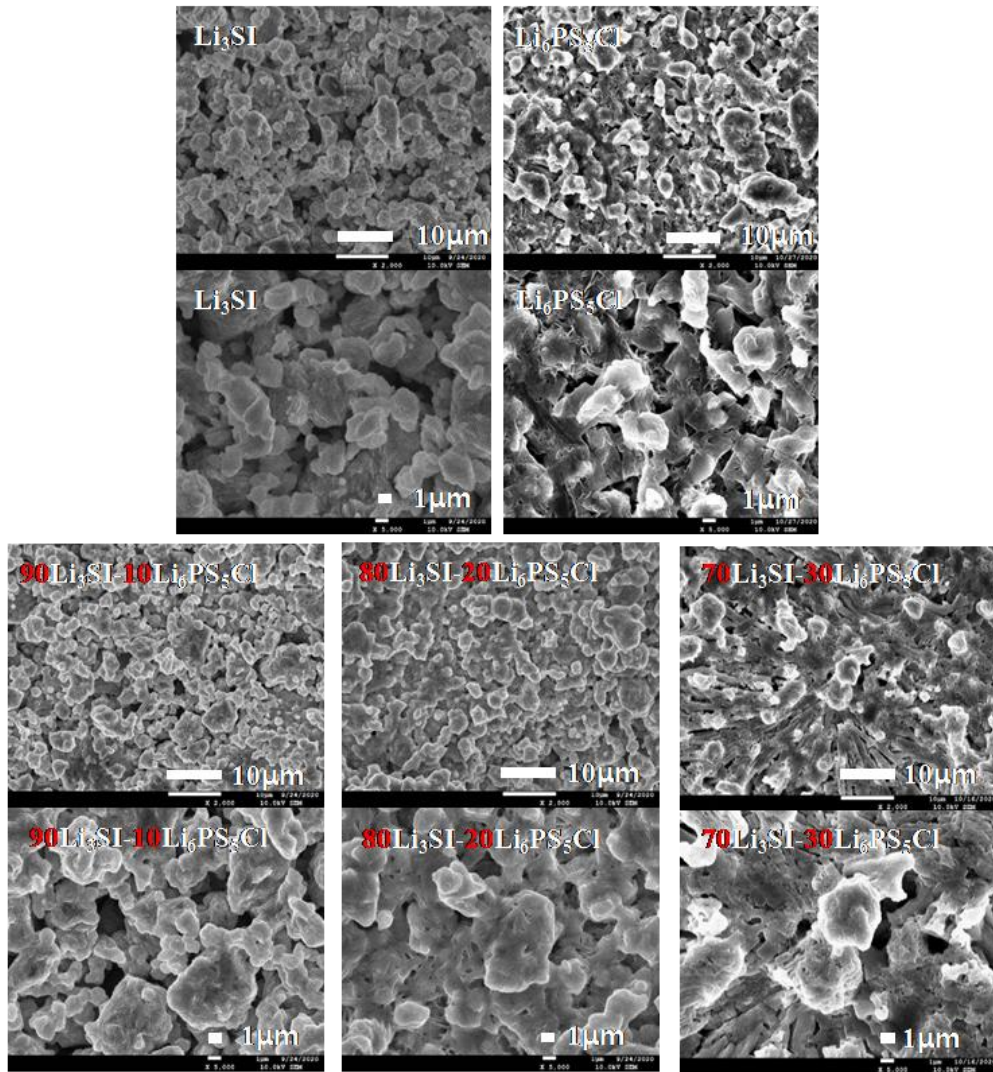


Figure. 3.3. SEM image for Li_3SI , $10\text{Li}_3\text{SI} - 90\text{Li}_6\text{PS}_5\text{Cl}$, $20\text{Li}_3\text{SI} - 80\text{Li}_6\text{PS}_5\text{Cl}$, $30\text{Li}_3\text{SI} - 70\text{Li}_6\text{PS}_5\text{Cl}$, and $\text{Li}_6\text{PS}_5\text{Cl}$.

3-3-1. Electrochemical measurements

Figure.4(a) shows the Nyquist plot of Li_3SI and mixed solid electrolytes. The equivalent circuit in Figure.4(a) means bulk resistance (R_1), grain boundary resistance of the electrolyte (R_2), solid electrolyte/indium interface resistance (R_3) and Warburg impedance (W)[39][40]. The ionic conductivity of Li_3SI was $6.12 \times 10^{-5} \text{S/cm}^{-1}$ at room temperature. Solid electrolytes mixed with $\text{Li}_6\text{PS}_5\text{Cl}$ ($3.85 \times 10^{-3} \text{S/cm}^{-1}$)[30][32] and Li_3SI . The semicircle in Nyquist plots is

due to charge transfer(R1) and grain boundary resistance(R2)[41]. The significant improvement in battery performance, as shown in figure.8, is due to the improved ionic conductivity of these solid electrolytes. The size of the semicircle decreases as the x value increases, which means that the resistance in ion transport decreases and the ionic conductivity increases. The ionic conductivity of $(100-x)\text{Li}_3\text{SI}-x\text{Li}_6\text{PS}_5\text{Cl}$ is $1.19 \times 10^{-4} \text{S/cm}^{-1}$ ($x=10$), $5.84 \times 10^{-4} \text{S/cm}^{-1}$ ($x=20$), $6.60 \times 10^{-4} \text{S/cm}^{-1}$ ($x=30$) at room temperature and the ionic conductivity increases as the ratio of $\text{Li}_6\text{PS}_5\text{Cl}$ increases. The activation energy of $(100-x)\text{Li}_3\text{SI}-x\text{Li}_6\text{PS}_5\text{Cl}$ ($x=0, 10, 20, \text{ and } 30$) for Li^+ ion conduction at the interface was analyzed using the measured ionic conductivity results in the temperature range of 25°C to 100°C . The activation energy can be calculated through Arrhenius equation $\sigma T = A \exp(-E_a/kT)$ in Figure. 5. The activation energy was calculated using the following equations (1) to (3) and the slope of the graph. The calculated values ranged from 0.29 eV to 0.34 eV, and were very similar to the calculated values of 0.27 eV of Li_3SI [23] and 0.33 to 0.35 eV of $\text{Li}_6\text{PS}_5\text{Cl}$ [42].

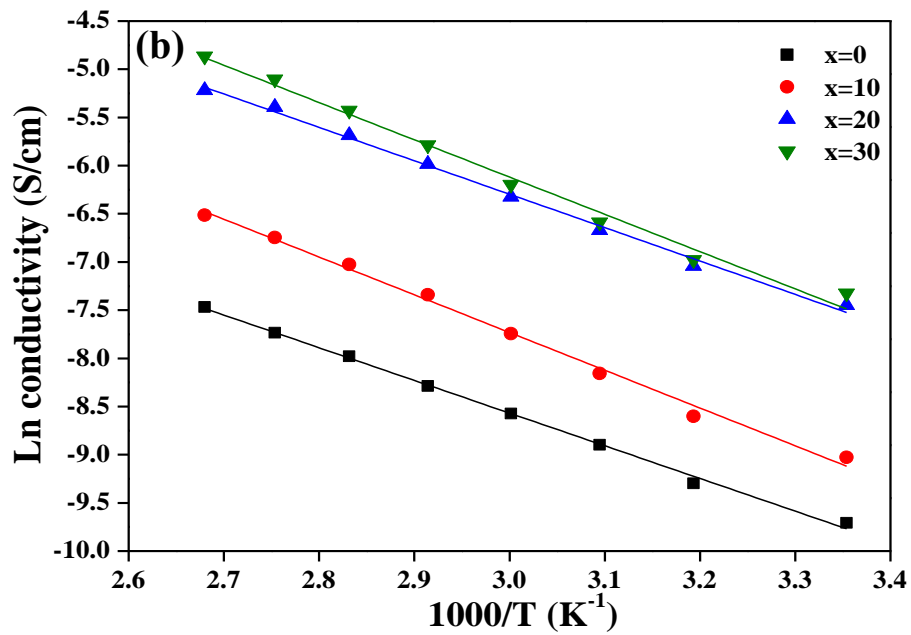
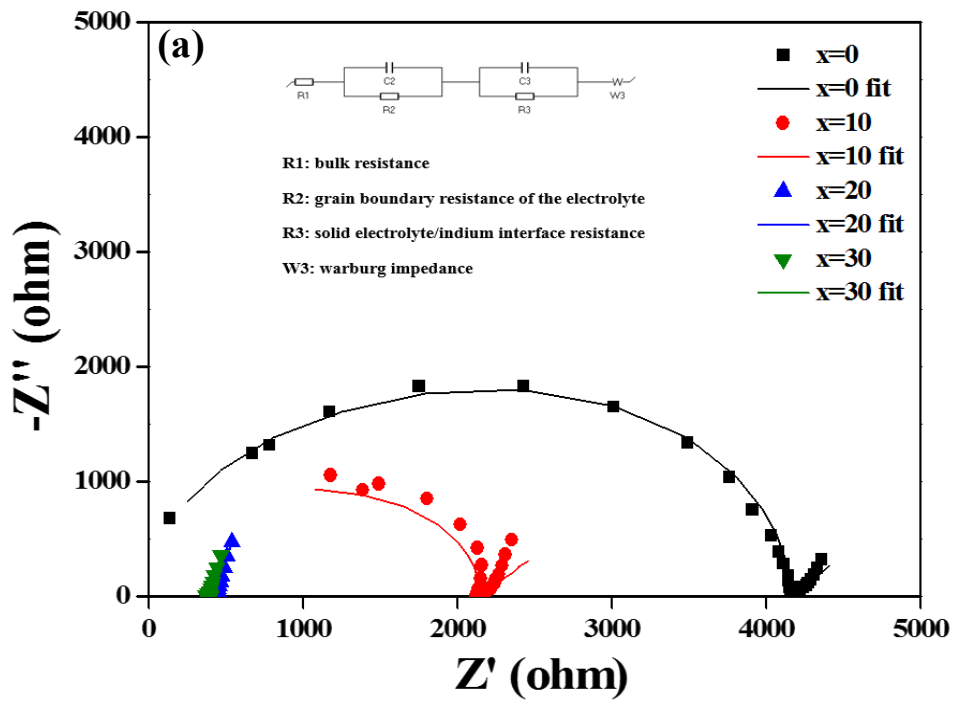


Figure. 3.4. Impedance profiles of (a) Nyquist plot of In | $\text{Li}_6\text{PS}_5\text{Cl}$ | In symmetric cell and (b) Arrhenius plots of the $(100-x)\text{Li}_3\text{SI}-x \text{Li}_6\text{PS}_5\text{Cl}$.

To evaluate the stability of the electrolytes for lithium metal, a CV curve was measured by applying 1mV/S in a potential range of -0.5 to 5V. CV curves of cells composed of stainless steel/(100-x)Li₃SI-xLi₆PS₅Cl/Li are shown on Figure.5 Lithium deposition ($\text{Li}^+ + \text{e}^- \rightarrow \text{Li}$) occurs at a cathodic current near 0V, and dissolution ($\text{Li} \rightarrow \text{Li}^+ + \text{e}^-$) occurs at anodic current. Except for 70Li₃SI-30Li₆PS₅Cl, all electrolytes showed stable curves without electrolyte decomposition at -0.5 to 5V vs Li/Li⁺, showing stability against lithium metal with an electrochemical window of 5V or higher. In the CV curve of 70Li₃SI-30Li₆PS₅Cl, a side reaction curve occurring at a potential in the range of -0.5 to 0V appears. This is because it contains more unconsumed Li₂S than other mixed electrolytes, so many side reaction species are generated at the interface between Li metal and solid electrolyte[43]. For this reason, the ionic conductivity of 70Li₃SI-30Li₆PS₅Cl is higher than that of other electrolytes, but we think that is the reason why the battery performance is lower than that of 80Li₃SI-20Li₆PS₅Cl(Figure. 8).

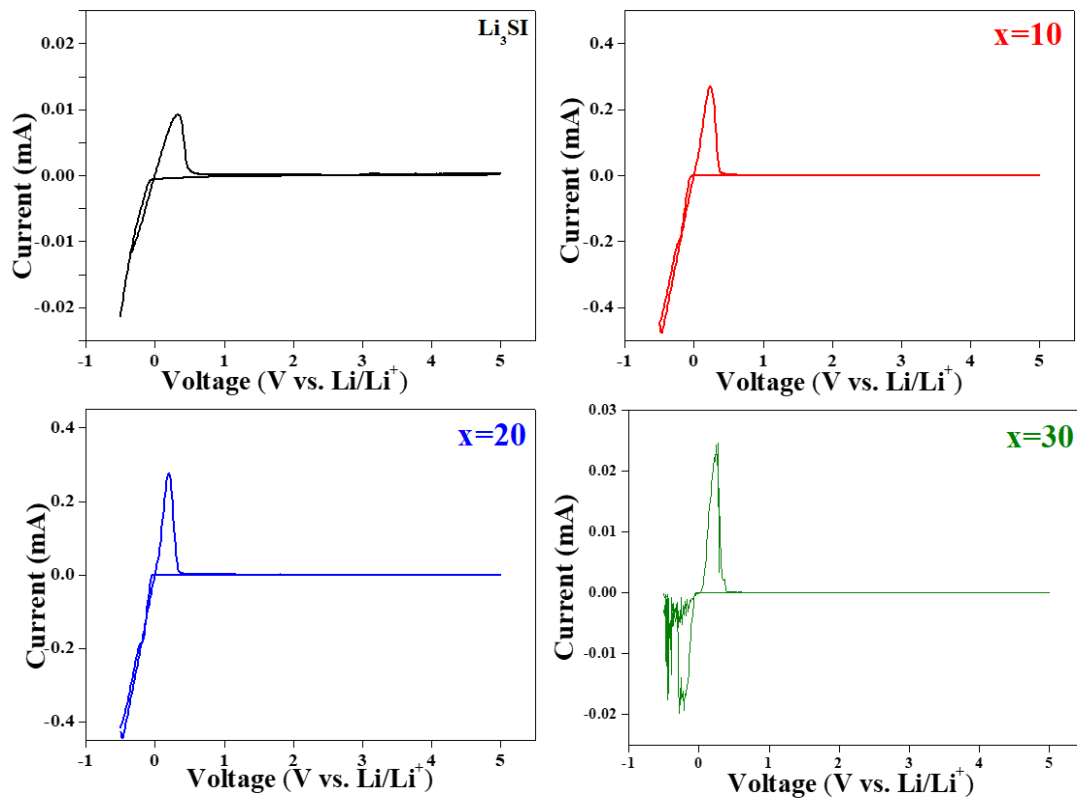


Figure. 3.5. Cyclic-voltammetry curve of $(100-x)\text{Li}_3\text{SI}-x\text{Li}_6\text{PS}_5\text{Cl}$ materials.

To confirm the stability between the lithium metal and the electrolyte, a DC-cycling test for 100 hours was performed by applying a current of 0.5 mA/cm^2 to a $\text{Li}/(100-x)\text{Li}_3\text{SI}-x\text{Li}_6\text{PS}_5\text{Cl}/\text{Li}$ symmetric cell. As shown on figure.6, Li_3SI shows a very stable cycle for 100 hours. This result means that it is very stable electrochemically and that lithium deposition in reaction with lithium occurs without any side reaction. The $(100-x)\text{Li}_3\text{SI}-x\text{Li}_6\text{PS}_5\text{Cl}$ mixed solid electrolytes maintain a high voltage profile compared to Li_3SI , so their stability is slightly lower than that of Li_3SI , but exhibits a stable cycle except for noise indicated during the initial cycle measurement. $10\text{Li}_3\text{SI}-90\text{Li}_6\text{PS}_5\text{Cl}$ shows noise during the measurement process until the initial 15th cycle, but in subsequent cycles, it shows a stable cycle without any side reaction, and $20\text{Li}_3\text{SI}-80\text{Li}_6\text{PS}_5\text{Cl}$ also maintains a constant voltage profile after the 30th cycle and shows a stable cycle. Among the mixed electrolytes, $20\text{Li}_3\text{SI}-80\text{Li}_6\text{PS}_5\text{Cl}$ shows the most stable lithium deposition with lithium metal, showing the best ASSLB battery performance as shown in figure.8. $30\text{Li}_3\text{SI}-70\text{Li}_6\text{PS}_5\text{Cl}$ shows a relatively stable cycle except that over-potential occurs due to side reactions at the 15th, 27th, 48th, and 77-82th cycles as the ratio of $\text{Li}_6\text{PS}_5\text{Cl}$ increases[44].

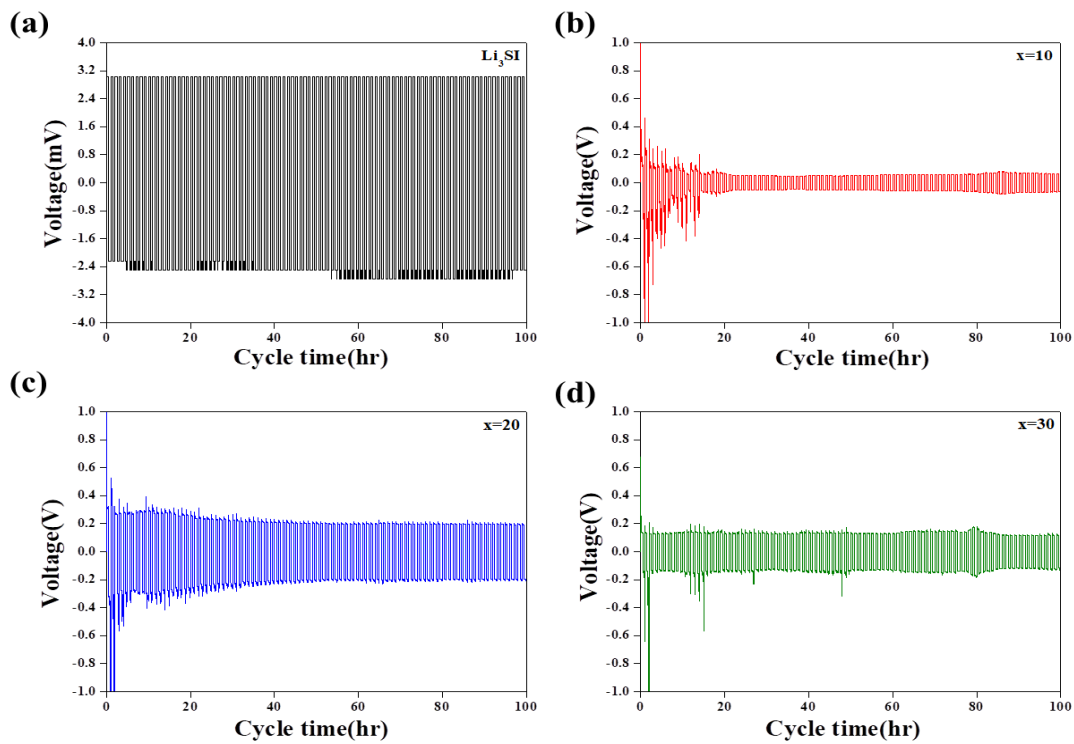


Figure. 3.6. DC cycling of $(100-x)\text{Li}_3\text{SI}-x \text{Li}_6\text{PS}_5\text{Cl}$ materials.

Impedance spectra were performed to measure the resistance of $\text{Li-In}/(100-x)\text{Li}_3\text{SI}-x\text{Li}_6\text{PS}_5\text{Cl}/\text{Li}(\text{Ni}_{0.8}\text{Co}_{0.1}\text{Mn}_{0.1})\text{O}_2$ composite ASSLB cells. Matches the equivalent circuit shown on figure.7 of the Nyquist plot, and R1: bulk resistance, R2: intergranular resistance, R3: positive/SE resistance, R4: negative/SE resistance[40][45]. As shown on figure.7, the first semicircle R3 is the resistance between Li-In/SE, and the second semicircle R4 is the resistance between cathode complex/SE[46]. The magnitude of the total resistance tends to decrease as $\text{Li}_6\text{PS}_5\text{Cl}$ is added, which is mostly consistent with the results in figure4. However, the size of the R3 resistance semicircles of $80\text{Li}_3\text{SI}-20 \text{Li}_6\text{PS}_5\text{Cl}$ and $70\text{Li}_3\text{SI}-30\text{Li}_6\text{PS}_5\text{Cl}$ is 184Ω and 158Ω , respectively, showing very little difference. As shown on figure.1 XRD diffraction patterns, the amount of Li_2S that was not consumed increases as the mixing ratio of $\text{Li}_6\text{PS}_5\text{Cl}$ increases, and accordingly, when the ASSLB cell is fabricated, the $70\text{Li}_3\text{SI}-30\text{Li}_6\text{PS}_5\text{Cl}$ R3 resistance is largely due to the increase of side reactions with lithium at the anode. The $70\text{Li}_3\text{SI}-30\text{Li}_6\text{PS}_5\text{Cl}$ has a higher ionic conductivity than $80\text{Li}_3\text{SI}-20\text{Li}_6\text{PS}_5\text{Cl}$, however, as the interfacial resistance between Li-In and the solid electrolyte increases, the Li deposition/dissolution is tricky, which degrades battery performance.

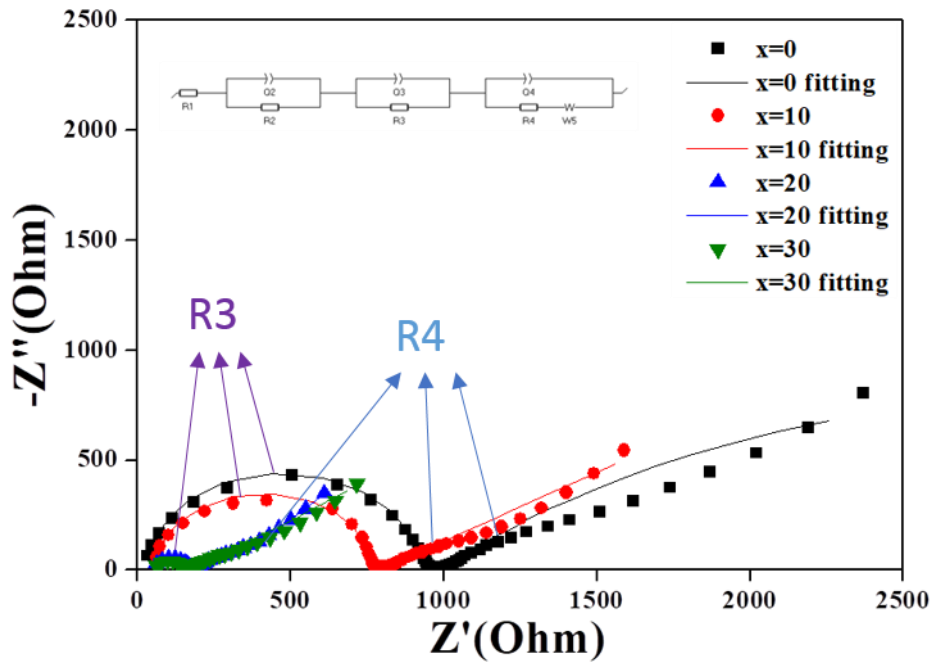


Figure. 3.7. Impedance profiles of Nyquist plot of Li-In alloy | $(100-x)\text{Li}_3\text{SI}-x\text{Li}_6\text{PS}_5\text{Cl}$

| $\text{Li}(\text{Ni}_{0.8}\text{Co}_{0.1}\text{Mn}_{0.1})\text{O}_2$ ASSLB cells.

Figure.8 shows the initial charge and discharge capacity of $\text{Li-In}/(100-x)\text{Li}_3\text{SI}-x\text{Li}_6\text{PS}_5\text{Cl}/\text{Li}(\text{Ni}_{0.8}\text{Co}_{0.1}\text{Mn}_{0.1})\text{O}_2$ composite ASSLB. Each full solid battery has an initial charge capacity of 141 ($x = 0$), 205 ($x = 10$), 233 ($x = 20$), 217 ($x = 30$), 237 ($x = 100$). The initial discharge capacity is 86 ($x = 0$), 144 ($x = 10$), 165 ($x = 20$), 153 ($x = 30$), 157 ($x = 100$) mAh/g. As shown on figure.4 and figure.7, battery performance is significantly improved compared to the case of using Li_3SI single solid electrolyte due to the improvement of ionic conductivity through mixing. In addition, the mixed solid electrolyte shows better performance by reducing the problem of contact resistance with the lithium metal that occurs in the $\text{Li}_6\text{PS}_5\text{Cl}$ single solid electrolyte[44]. $80\text{Li}_3\text{SI}-20\text{Li}_6\text{PS}_5\text{Cl}$ mixed solid electrolyte has lower ionic conductivity than $\text{Li}_6\text{PS}_5\text{Cl}$, $70\text{Li}_3\text{SI}-30\text{Li}_6\text{PS}_5\text{Cl}$, but $80\text{Li}_3\text{SI}-20\text{Li}_6\text{PS}_5\text{Cl}$ improves stability against lithium metal, providing excellent all-solid battery performance. This is consistent with the result of the side reaction of $70\text{Li}_3\text{SI}-30\text{Li}_6\text{PS}_5\text{Cl}$ to lithium metal shown in the CV curve of figure.5. Figure.9 (a), (b), and (c) show the battery cycle performance of ASSLBs up to 30 cycles. Figure.9(a) shows the discharge capacity up to 30 times, and each discharge capacity at 30 times is 59 ($x = 0$), 113 ($x = 10$), 132 ($x = 20$), 122 ($x = 30$), and 99 ($x = 100$). Besides, in the cycle holding graph in figure.9(b), the cycle stability of the mixed solid electrolyte is better than that of the single solid electrolyte. It can be seen that not only the internal resistance decreased due to the improvement of ionic conductivity through the mixing of the solid electrolyte, but also the performance of the entire solid-state battery was improved due to the increased stability with lithium metal. Compared to the whole solid battery composed of Li_3SI and $\text{Li}_6\text{PS}_5\text{Cl}$ single electrolyte, the battery composed of mixed solid electrolyte $(100-x)\text{Li}_3\text{SI}-x\text{Li}_6\text{PS}_5\text{Cl}$ can be seen to maintain better discharge capacity after 30 cycles, especially best with $80\text{Li}_3\text{SI}-20\text{Li}_6\text{PS}_5\text{Cl}$. You can check that the discharge capacity is maintained. This proves that $80\text{Li}_3\text{SI}-20\text{Li}_6\text{PS}_5\text{Cl}$ is the most optimal mixing ratio with improved ionic conductivity than Li_3SI and improved stability to lithium metal than $\text{Li}_6\text{PS}_5\text{Cl}$. Figure.9(c) shows a graph of Coulomb efficiency for up to 30 cycles. All initial coulombic efficiencies are low due to the initial resistance between electrode and electrolyte[47][48]. Not only single electrolytes but also mixed solid

electrolytes exhibit excellent coulombic efficiency.

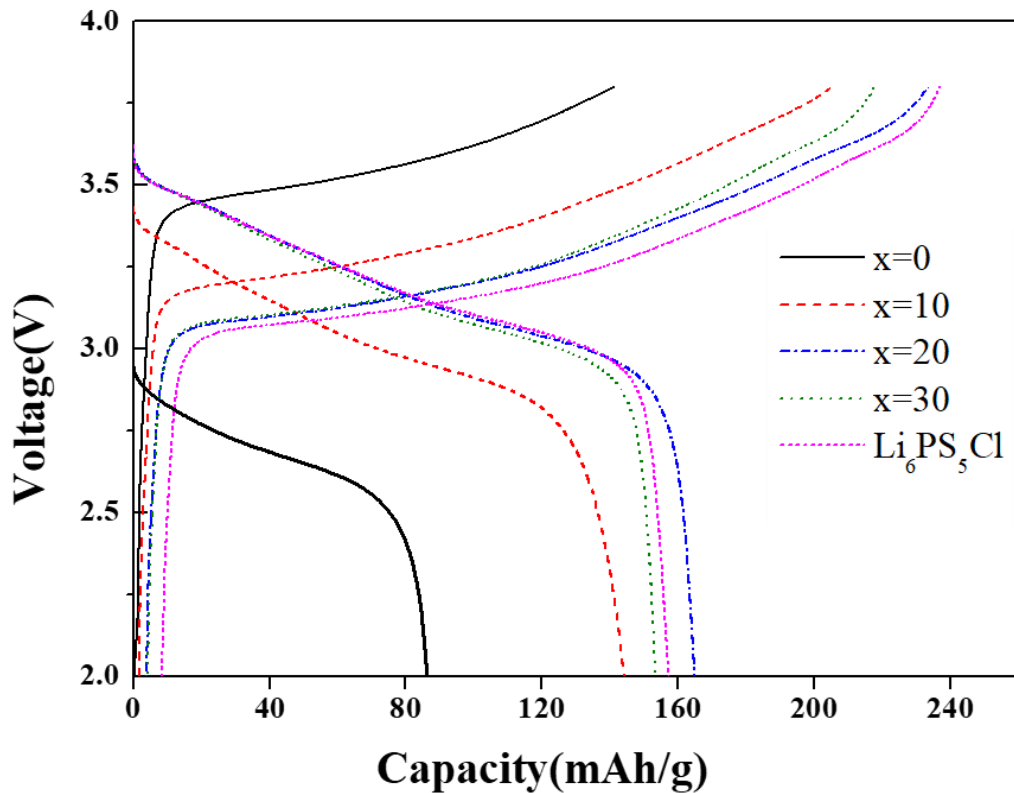


Figure. 3.8. Initial cycle curve of Li-In alloy | $(100-x)\text{Li}_3\text{SI}-x\text{Li}_6\text{PS}_5\text{Cl}$ | $\text{Li}(\text{Ni}_{0.8}\text{Co}_{0.1}\text{Mn}_{0.1})\text{O}_2$ ASSLB.

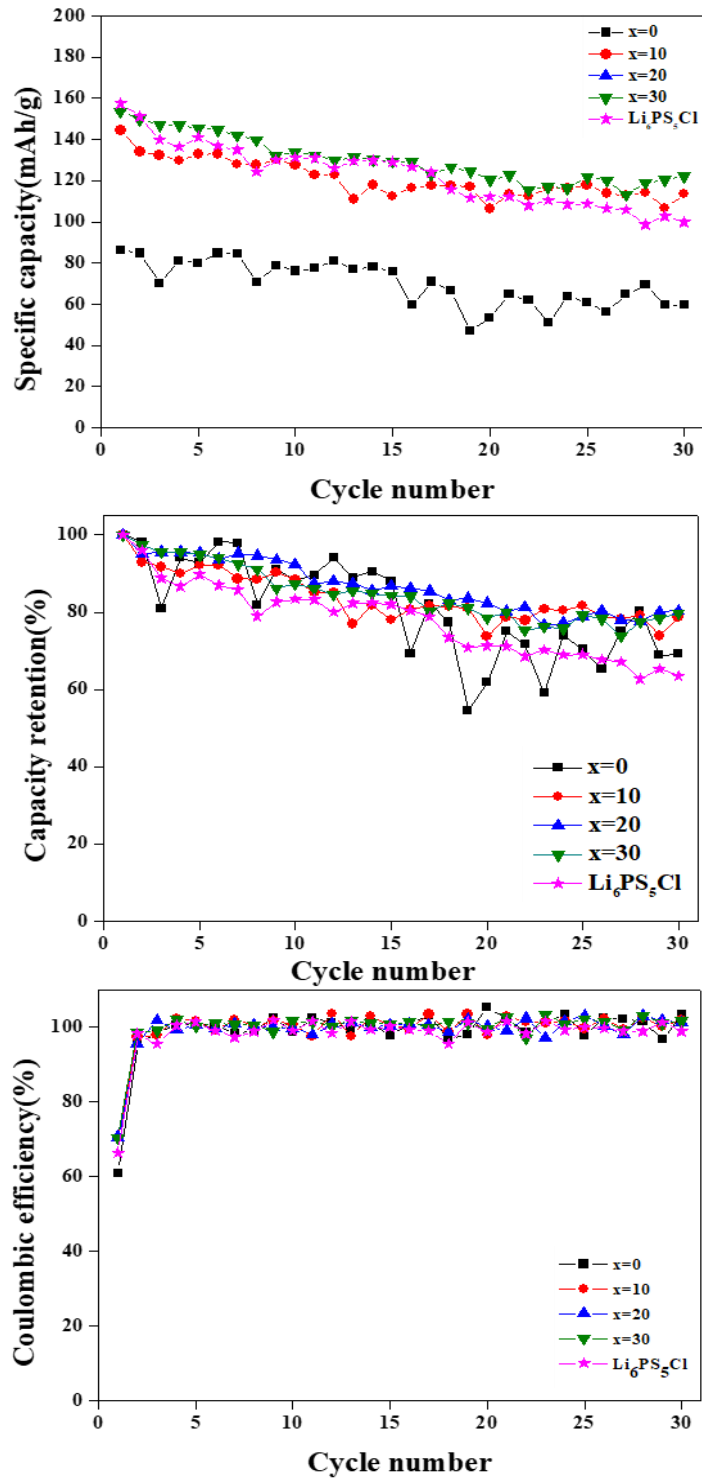


Figure. 3.9. (a) Cycle performance, (b) capacity retention, and (c) Coulombic efficiency of Li-In alloy | (100-x)Li₃SI-xLi₆PS₅Cl | Li(Ni_{0.8}Co_{0.1}Mn_{0.1})O₂ ASSLB.

4. Conclusions

After each of the Li_3SI and $\text{Li}_6\text{PS}_5\text{Cl}$, solid electrolytes were prepared, a $(100-x)\text{Li}_3\text{SI}-x\text{Li}_6\text{PS}_5\text{Cl}$ ($x=0, 10, 20,$ and 30) having the stability of Li_3SI with lithium metal and the high ionic conductivity of $\text{Li}_6\text{PS}_5\text{Cl}$ was prepared through a mechanical ball mill process. As the x value increased, it was confirmed that the amorphous argyrodite peak before annealing appeared in the XRD pattern and that the Li_3SI peak gradually increased. When argyrodite is gradually added, the ionic conductivity increases, and especially when $x=30$, it has a relatively high ion conductivity of $6.60 \times 10^{-4} \text{S/cm}$. However, when $x=30$, noise can be checked below 0V , as can be seen in CV measurement. In the DC-Cycling test conducted to evaluate compatibility and stability with lithium metal, some noise was generated, but it was confirmed that the cycle proceeded stably for 100 hours at a high current density of 1mA/cm^2 . In addition, ion conductivity increased due to the addition of argyrodite, resulting in ASSLBs ($\text{Li-In}/(100-x)\text{Li}_3\text{SI}-x\text{Li}_6\text{PS}_5\text{Cl}$ ($x=0, 10, 20,$ and 30)/ $\text{Li}(\text{Ni}_{0.8}\text{Co}_{0.1}\text{Mn}_{0.1})\text{O}_2$ composites) show excellent performance, especially, in $80\text{Li}_3\text{SI}-20\text{Li}_6\text{PS}_5\text{Cl}$ with the highest capacity (165mAh/g) and the best cycle stability. This result confirms that the ASSLB cell using $80\text{Li}_3\text{SI}-20\text{Li}_6\text{PS}_5\text{Cl}$ shows better battery performance than the ASSLB cell using argyrodite single solid electrolyte. Therefore, it was confirmed that mixing a certain amount of $\text{Li}_6\text{PS}_5\text{Cl}$ and Li_3SI helps improve battery performance while maintaining stability with Li metal.

References

- [1] X. Yao *et al.*, “All-solid-state lithium batteries with inorganic solid electrolytes: Review of fundamental science,” *Chinese Phys. B*, vol. 25, no. 1, 2015.
- [2] J. R. D. and D. S. W. Wu Li, “Rechargeable Lithium Batteries with Aqueous Electrolytes,” *Am. Assoc. Adv. Sci.*, vol. 264, no. 5162, pp. 1115–1118, 2016.
- [3] P. Verma, P. Maire, and P. Novák, “A review of the features and analyses of the solid electrolyte interphase in Li-ion batteries,” *Electrochim. Acta*, vol. 55, no. 22, pp. 6332–6341, 2010.
- [4] A. Abouimrane, J. Ding, and I. J. Davidson, “Liquid electrolyte based on lithium bis-fluorosulfonyl imide salt: Aluminum corrosion studies and lithium ion battery investigations,” *J. Power Sources*, vol. 189, no. 1, pp. 693–696, 2009.
- [5] T. Baba and Y. Kawamura, “Structure and ionic conductivity of $\text{Li}_2\text{S}-\text{P}_2\text{S}_5$ glass electrolytes simulated with first-principles molecular dynamics,” *Front. Energy Res.*, vol. 4, no. JUN, pp. 1–10, 2016.
- [6] A. Manthiram, X. Yu, and S. Wang, “Lithium battery chemistries enabled by solid-state electrolytes,” *Nat. Rev. Mater.*, vol. 2, no. 4, pp. 1–16, 2017.
- [7] K. Takada, “Progress and prospective of solid-state lithium batteries,” *Acta Mater.*, vol. 61, no. 3, pp. 759–770, 2013.
- [8] H. Wan, G. Peng, X. Yao, J. Yang, P. Cui, and X. Xu, “ $\text{Cu}_2\text{ZnSnS}_4$ /graphene nanocomposites for ultrafast, long life all-solid-state lithium batteries using lithium metal anode,” *Energy Storage Mater.*, vol. 4, pp. 59–65, 2016.
- [9] S. Wenzel, S. J. Sedlmaier, C. Dietrich, W. G. Zeier, and J. Janek, “Interfacial reactivity and interphase growth of argyrodite solid electrolytes at lithium metal electrodes,” *Solid State Ionics*, vol. 318, no. February 2017, pp. 102–112, 2018.
- [10] K. Kataoka, H. Nagata, and J. Akimoto, “Lithium-ion conducting oxide single crystal as solid electrolyte for advanced lithium battery application,” *Sci. Rep.*, vol. 8, no. 1, pp. 13–15, 2018.
- [11] S. Ohta, T. Kobayashi, J. Seki, and T. Asaoka, “Electrochemical performance of an all-solid-state lithium ion battery with garnet-type oxide electrolyte,” *J. Power Sources*, vol. 202, pp. 332–335, 2012.
- [12] A. Yamauchi, A. Sakuda, A. Hayashi, and M. Tatsumisago, “Preparation and ionic conductivities of $(100 - X)(0.75\text{Li} 2\text{S} \cdot 0.25\text{P}_2\text{S}_5) \cdot x\text{LiBH}_4$ glass electrolytes,” *J. Power Sources*, vol. 244, pp. 707–710, 2013.
- [13] B. Huang, X. Yao, Z. Huang, Y. Guan, Y. Jin, and X. Xu, “ Li_3PO_4 -doped $\text{Li}_7\text{P}_3\text{S}_{11}$

- glass-ceramic electrolytes with enhanced lithium ion conductivities and application in all-solid-state batteries,” *J. Power Sources*, vol. 284, pp. 206–211, 2015.
- [14] S. Choi, M. Eom, C. Park, S. Son, G. Lee, and D. Shin, “Effect of Li_2SO_4 on the properties of $\text{Li}_2\text{S}-\text{P}_2\text{S}_5$ glass-ceramic solid electrolytes,” *Ceram. Int.*, vol. 42, no. 6, pp. 6738–6742, 2016.
- [15] Z. Zhu, I. H. Chu, and S. P. Ong, “ $\text{Li}_3\text{Y}(\text{PS}_4)_2$ and $\text{Li}_5\text{PS}_4\text{Cl}_2$: New Lithium Superionic Conductors Predicted from Silver Thiophosphates using Efficiently Tiered Ab Initio Molecular Dynamics Simulations,” *Chem. Mater.*, vol. 29, no. 6, pp. 2474–2484, 2017.
- [16] P. Lu, F. Ding, Z. Xu, J. Liu, X. Liu, and Q. Xu, “Study on $(100-x)(70\text{Li}_2\text{S}-30\text{P}_2\text{S}_5)-x\text{Li}_2\text{ZrO}_3$ glass-ceramic electrolyte for all-solid-state lithium-ion batteries,” *J. Power Sources*, vol. 356, pp. 163–171, 2017.
- [17] Y. Sun, K. Suzuki, S. Hori, M. Hirayama, and R. Kanno, “Superionic Conductors: $\text{Li}_{10+\delta}[\text{Sn}_y\text{Si}_{1-y}]_{1+\delta}\text{P}_2-\delta\text{S}_{12}$ with a $\text{Li}_{10}\text{GeP}_2\text{S}_{12}$ -type Structure in the Li_3PS_4 - Li_4SnS_4 - Li_4SiS_4 Quasi-ternary System,” *Chem. Mater.*, vol. 29, no. 14, pp. 5858–5864, 2017.
- [18] R. F. Indrawan, T. Yamamoto, H. H. P. Nguyen, H. Muto, and A. Matsuda, “Liquid-phase synthesis of $100\text{Li}_3\text{PS}_4-50\text{LiI}-x\text{Li}_3\text{PO}_4$ solid electrolytes,” *Solid State Ionics*, vol. 345, no. July 2019, p. 115184, 2020.
- [19] A. Emly, E. Kioupakis, and A. Van Der Ven, “Phase stability and transport mechanisms in antiperovskite Li_3OCl and Li_3OBr superionic conductors,” *Chem. Mater.*, vol. 25, no. 23, pp. 4663–4670, 2013.
- [20] X. Lü *et al.*, “Li-rich anti-perovskite Li_3OCl films with enhanced ionic conductivity,” *Chem. Commun.*, vol. 50, no. 78, pp. 11520–11522.
- [21] M. H. Chen, A. Emly, and A. Van Der Ven, “Anharmonicity and phase stability of antiperovskite Li_3OCl ,” *Phys. Rev. B - Condens. Matter Mater. Phys.*, vol. 91, no. 21, pp. 1–8, 2015.
- [22] L. Yin *et al.*, “Synthesis of Antiperovskite Solid Electrolytes: Comparing Li_3SI , Na_3SI , and Ag_3SI ,” *Inorg. Chem.*, vol. 59, no. 16, pp. 11244–11247, 2020.
- [23] Z. Wang, H. Xu, M. Xuan, and G. Shao, “From anti-perovskite to double anti-perovskite: Tuning lattice chemistry to achieve super-fast Li^+ transport in cubic solid lithium halogen-chalcogenides,” *J. Mater. Chem. A*, vol. 6, no. 1, pp. 73–83, 2017.
- [24] R. P. Rao and S. Adams, “Studies of lithium argyrodite solid electrolytes for all-solid-state batteries,” *Phys. Status Solidi Appl. Mater. Sci.*, vol. 208, no. 8, pp. 1804–1807, 2011.
- [25] I. P. Studenyak *et al.*, “The effect of temperature and pressure on the optical absorption edge in $\text{Cu}_6\text{PS}_5\text{X}$ ($\text{X} = \text{Cl}, \text{Br}, \text{I}$) crystals,” *J. Phys. Chem. Solids*, vol. 60, no. 12, pp. 1897–1904, 1999.

- [26] M. Kranjčec, I. P. Studenyak, R. Y. Buchuk, V. O. Stephanovich, S. Kökényesi, and M. Kis-Varga, “Structural properties and Raman scattering in $\text{Cu}_6\text{PS}_5\text{X}$ ($\text{X} = \text{I}, \text{Br}$) nanocrystalline solid electrolytes,” *Solid State Ionics*, vol. 179, no. 1–6, pp. 218–221, 2008.
- [27] R. B. Beeken, J. J. Garbe, J. M. Gillis, N. R. Petersen, B. W. Podoll, and M. R. Stoneman, “Electrical conductivities of the $\text{Ag}_6\text{PS}_5\text{X}$ and the $\text{Cu}_6\text{PSe}_5\text{X}$ ($\text{X} = \text{Br}, \text{I}$) argyrodites,” *J. Phys. Chem. Solids*, vol. 66, no. 5, pp. 882–886, 2005.
- [28] A. Gagor, A. Pietraszko, and D. Kaynts, “Structural aspects of fast copper mobility in $\text{Cu}_6\text{PS}_5\text{Cl}$ -The best solid electrolyte from $\text{Cu}_6\text{PS}_5\text{X}$ series,” *J. Solid State Chem.*, vol. 181, no. 4, pp. 777–782, 2008.
- [29] I. P. Studenyak, “Optical absorption edge and luminescence in phosphorous-implanted $\text{Cu}_6\text{PS}_5\text{X}$ ($\text{X} = \text{I}, \text{Br}$) single crystals,” *Semicond. Phys. Quantum Electron. Optoelectron.*, vol. 14, no. 3, pp. 287–293, 2011.
- [30] H.-J. Deiseroth *et al.*, “ $\text{Li}_6\text{PS}_5\text{X}$: A Class of Crystalline Li-Rich Solids With an Unusually High Li^+ Mobility,” *Angew. Chemie*, vol. 120, no. 4, pp. 767–770, 2008.
- [31] S. Chen *et al.*, “Sulfide solid electrolytes for all-solid-state lithium batteries: Structure, conductivity, stability and application,” *Energy Storage Mater.*, vol. 14, no. December 2017, pp. 58–74, 2018.
- [32] M. A. Kraft *et al.*, “Influence of Lattice Polarizability on the Ionic Conductivity in the Lithium Superionic Argyrodites $\text{Li}_6\text{PS}_5\text{X}$ ($\text{X} = \text{Cl}, \text{Br}, \text{I}$),” *J. Am. Chem. Soc.*, vol. 139, no. 31, pp. 10909–10918, 2017.
- [33] S. Yubuchi, M. Uematsu, M. Deguchi, A. Hayashi, and M. Tatsumisago, “Lithium-Ion-Conducting Argyrodite-Type $\text{Li}_6\text{PS}_5\text{X}$ ($\text{X} = \text{Cl}, \text{Br}, \text{I}$) Solid Electrolytes Prepared by a Liquid-Phase Technique Using Ethanol as a Solvent,” *ACS Appl. Energy Mater.*, vol. 1, no. 8, pp. 3622–3629, 2018.
- [34] A. R. Stamminger, B. Ziebarth, M. Mrovec, T. Hammerschmidt, and R. Drautz, “Ionic Conductivity and Its Dependence on Structural Disorder in Halogenated Argyrodites $\text{Li}_6\text{PS}_5\text{X}$ ($\text{X} = \text{Br}, \text{Cl}, \text{I}$),” *Chem. Mater.*, 2019.
- [35] J. Auvergniot, A. Cassel, J. B. Ledeuil, V. Viallet, V. Seznec, and R. Dedryvère, “Interface Stability of Argyrodite $\text{Li}_6\text{PS}_5\text{Cl}$ toward LiCoO_2 , $\text{LiNi}_{1/3}\text{Co}_{1/3}\text{Mn}_{1/3}\text{O}_2$, and LiMn_2O_4 in Bulk All-Solid-State Batteries,” *Chem. Mater.*, vol. 29, no. 9, pp. 3883–3890, 2017.
- [36] C. Yu, L. van Eijck, S. Ganapathy, and M. Wagemaker, “Synthesis, structure and electrochemical performance of the argyrodite $\text{Li}_6\text{PS}_5\text{Cl}$ solid electrolyte for Li-ion solid state batteries,” *Electrochim. Acta*, vol. 215, pp. 93–99, 2016.
- [37] J. Zhang *et al.*, “All-solid-state batteries with slurry coated $\text{LiNi}_{0.8}\text{Co}_{0.1}\text{Mn}_{0.1}\text{O}_2$ composite cathode and $\text{Li}_6\text{PS}_5\text{Cl}$ electrolyte: Effect of binder content,” *J. Power*

- Sources*, vol. 391, no. February, pp. 73–79, 2018.
- [38] E. P. Kamphaus and P. B. Balbuena, “Polysulfide reduction and Li_2S phase formation in the presence of lithium metal and solid electrolyte interphase layer,” *J. Power Sources*, no. November, p. 229289, 2020.
- [39] W. Zhang *et al.*, “Interfacial Processes and Influence of Composite Cathode Microstructure Controlling the Performance of All-Solid-State Lithium Batteries,” *ACS Appl. Mater. Interfaces*, vol. 9, no. 21, pp. 17835–17845, 2017.
- [40] G. Oh, M. Hirayama, O. Kwon, K. Suzuki, and R. Kanno, “Bulk-Type All Solid-State Batteries with 5 v Class $\text{LiNi}_{0.5}\text{Mn}_{1.5}\text{O}_4$ Cathode and $\text{Li}_{10}\text{GeP}_2\text{S}_{12}$ Solid Electrolyte,” *Chem. Mater.*, vol. 28, no. 8, pp. 2634–2640, 2016.
- [41] X. Yao *et al.*, “High-Performance All-Solid-State Lithium–Sulfur Batteries Enabled by Amorphous Sulfur-Coated Reduced Graphene Oxide Cathodes,” *Adv. Energy Mater.*, vol. 7, no. 17, pp. 1–9, 2017.
- [42] C. Yu *et al.*, “Facile Synthesis toward the Optimal Structure-Conductivity Characteristics of the Argyrodite $\text{Li}_6\text{PS}_5\text{Cl}$ Solid-State Electrolyte,” *ACS Appl. Mater. Interfaces*, vol. 10, no. 39, pp. 33296–33306, 2018.
- [43] C. Lai *et al.*, “Stabilizing a Lithium Metal Battery by an in Situ Li_2S -modified Interfacial Layer via Amorphous-Sulfide Composite Solid Electrolyte,” *Nano Lett.*, 2020.
- [44] J. Zhang *et al.*, “Poly(ethylene oxide) reinforced $\text{Li}_6\text{PS}_5\text{Cl}$ composite solid electrolyte for all-solid-state lithium battery: Enhanced electrochemical performance, mechanical property and interfacial stability,” *J. Power Sources*, vol. 412, no. October 2018, pp. 78–85, 2019.
- [45] A. Sharafi, C. G. Haslam, R. D. Kerns, J. Wolfenstine, and J. Sakamoto, “Controlling and correlating the effect of grain size with the mechanical and electrochemical properties of $\text{Li}_7\text{La}_3\text{Zr}_2\text{O}_{12}$ solid-state electrolyte,” *J. Mater. Chem. A*, vol. 5, no. 40, pp. 21491–21504, 2017.
- [46] X. Li *et al.*, “In/ex-situ Raman spectra combined with EIS for observing interface reactions between Ni-rich layered oxide cathode and sulfide electrolyte,” *J. Energy Chem.*, vol. 48, pp. 195–202, 2020.
- [47] H. Wan *et al.*, “Nanoscaled Na_3PS_4 Solid Electrolyte for All-Solid-State FeS_2/Na Batteries with Ultrahigh Initial Coulombic Efficiency of 95% and Excellent Cyclic Performances,” *ACS Appl. Mater. Interfaces*, vol. 10, no. 15, pp. 12300–12304, 2018.
- [48] J. E. Trevey, Y. S. Jung, and S. H. Lee, “Preparation of $\text{Li}_2\text{S}-\text{GeSe}_2-\text{P}_2\text{S}_5$ electrolytes by a single step ball milling for all-solid-state lithium secondary batteries,” *J. Power Sources*, vol. 195, no. 15, pp. 4984–4989, 2010.

Chapter 5. Summary

We studied a solid electrolyte mixed with anti-perovskite Li_3SI and argyrodite $\text{Li}_6\text{PS}_5\text{Cl}$ to increase battery performance by improving the ionic conductivity of solid electrolytes and stability against lithium metal.

The mixed solid electrolyte we studied is $(100-x)\text{Li}_3\text{SI}-x\text{Li}_6\text{PS}_5\text{Cl}$, which is mixed with anti-perovskite Li_3SI and argyrodite $\text{Li}_6\text{PS}_5\text{Cl}$ in a certain molar ratio. These mixed solid electrolytes were synthesized and mixed through a mechanical ball mill process. As shown on the mixed XRD pattern, it was confirmed that as x increased, the intensity of the main peak of Li_3SI decreased and the intensity of the main peak of $\text{Li}_6\text{PS}_5\text{Cl}$ (before annealing) increased. This is because $\text{Li}_6\text{PS}_5\text{Cl}$, which has undergone a crystallization process through annealing, becomes amorphous again during the mixing process through a mechanical ball mill process, and a peak of $\text{Li}_6\text{PS}_5\text{Cl}$ (before annealing) appears. As a result of electrochemical experiments, it was confirmed that $\text{Li}_6\text{PS}_5\text{Cl}$ has high ionic conductivity ($3.85 \times 10^{-3} \text{S/cm}$), so the ionic conductivity increases as it is added. However, since $\text{Li}_6\text{PS}_5\text{Cl}$ has poor stability against lithium metal, it was confirmed that noise occurs below 0V of CV measurement when $x=30$. Based on these data, we predicted that the best battery performance when $x=20$, which has relatively high ionic conductivity and no problem in terms of stability against lithium metal, manufactured ASSLB and conducted a cycle test. ASSLB is manufactured in the form of $\text{Li-In alloy} \mid (100-x)\text{Li}_3\text{SI}-x\text{Li}_6\text{PS}_5\text{Cl} \mid \text{Li}(\text{Ni}_{0.8}\text{Co}_{0.1}\text{Mn}_{0.1})\text{O}_2$. The results of the ASSLB cycle test resulted in results that match what we expected. It was confirmed that it has the best cycle stability and discharge capacity (165mAh/g) when $x=20$. Therefore, when a certain amount of $\text{Li}_6\text{PS}_5\text{Cl}$ is added to Li_3SI , synergistic effects of high ionic conductivity, which is the advantage of $\text{Li}_6\text{PS}_5\text{Cl}$, and stability with lithium metal, which is an advantage of anti-perovskite, can be obtained. The $(100-x)\text{Li}_3\text{SI}-x\text{Li}_6\text{PS}_5\text{Cl}$ electrolytes that mixes the two materials improves the electrochemical performance, and 80 Li_3SI -20 $\text{Li}_6\text{PS}_5\text{Cl}$ in particular could be a promising candidate as a solid electrolyte for ASSLB.